Mechanisms controlling the plasma membrane targeting and the nanodomain organization of the plant SPFH protein HIR2

Michal Daněk, Omar Hdedeh, Jesús Amo, Jessica Boutet, Michaela Neubergerová, Héla Safi, Anas Abuzeineh, Amanda Martín-barranco, Jean-bernard Fiche, Caroline Mercier, et al.

the plant journal

SEB SOCIETY FOR EXPERIMENTAL BIOLOGY

The Plant Journal (2026) **126,** e70879 doi: 10.1111/tpj.70879

Mechanisms controlling the plasma membrane targeting and the nanodomain organization of the plant SPFH protein HIR2

Michal Daněk[1,2,#], Omar Hdedeh[1,#], Jesús Amo[1,#], Jessica Boutet[1], Michaela Neubergerová[2,3], Héla Safi[1], Anas Abuzeineh[1], Amanda Martín-Barranco[4], Jean-Bernard Fiche[5], Caroline Mercier[1], Baldwin Dumortier[1,6], Gabriel Krouk[1], Marcelo Nollmann[5], Roman Pleskot[2], Yohann Boutté[7], Véronique Santoni[1], Sébastien Mongrand[7], Alexandre Martinière[1] and Enric Zelazny[1,*]

[1]*Institute for Plant Sciences of Montpellier (IPSiM), CNRS, Univ. Montpellier, INRAE, Institut Agro, 34060 Montpellier, France,*
[2]*Institute of Experimental Botany, Czech Academy of Sciences, Rozvojová 263, 165 00 Prague, Czech Republic,*
[3]*Department of Experimental Plant Biology, Faculty of Science, Charles University in Prague, Prague, Czech Republic,*
[4]*Institute for Integrative Biology of the Cell (I2BC), UMR9198 CNRS/CEA/Univ. Paris Sud, Université Paris-Saclay, 91198 Gif-sur-Yvette, France,*
[5]*Centre de Biologie Structurale, CNRS, UMR 5048, Inserm U1054, Univ. Montpellier, 34090 Montpellier, France,*
[6]*Institut Montpelliérain Alexander Grothendieck (IMAG), UMR 5149, Montpellier, France, and*
[7]*Laboratoire de Biogenèse Membranaire LBM, UMR 5200, CNRS and University of Bordeaux, 33140 Villenave d'Ornon, France*

Received 24 September 2025; revised 23 March 2026; accepted 1 April 2026.
*For correspondence (e-mail enric.zelazny@cnrs.fr).
#These authors contributed equally to this work.

SUMMARY

Plasma membranes (PM) contain myriads of diverse nanodomains that correspond to nanometric scale structures enriched in specific lipids and proteins acting as signaling/regulation hubs involved in diverse biological processes. So far, how PM nanodomains are formed and maintained in plant cells remains largely unknown. We sought to address this question using HIR2, a plant-specific Stomatin/Prohibitin/Flotillin/HflK/C (SPFH) domain-containing protein that arranges in PM nanodomains, as a model. We revealed that the mono S-acylation of Arabidopsis HIR2 either on C6 or on C7 was required for the localization of HIR2 in the PM. In addition, using state-of-the-art microscopy techniques, we provided evidence that the lipid composition in sterols and very long chain fatty acids of the PM influenced HIR2 nanodomain organization. Interestingly, we highlighted that the oligomerization of HIR2 through its C-terminal domain is essential for its organization in nanodomains and to ensure HIR2 lateral stability in the PM. HIR proteins are involved in plant immunity, and we revealed here that HIR2 nanodomain organization is required to boost the apoplastic reactive oxygen species burst induced by the bacterial peptide flg22. Overall, we propose that HIR2 nanodomain organization is a complex mechanism relying on different parameters and is essential for HIR2 function.

Keywords: plasma membrane nanodomains, HIR2, S-acylation, lipids, oligomerization, super-resolution microscopy, reactive oxygen species (ROS), *Arabidopsis thaliana*.

INTRODUCTION

Plant plasma membranes (PM) contain myriads of diverse domains at nanometer scale size (20 nm to 1 μm) termed nanodomains that correspond to the functional assembly of specific proteins and lipids (Jaillais et al., 2024; Jaillais & Ott, 2020; Jarsch et al., 2014; Martiniere & Zelazny, 2021). Although the molecular function of nanodomains remains largely unknown, they emerge as signaling/regulatory platforms gathering proteins involved in various cellular processes (Bucherl et al., 2017; Demir et al., 2013; Gronnier et al., 2017; Liu, Yeh, et al., 2024; Platre et al., 2019; Smokvarska et al., 2020). The Stomatin/Prohibitin/Flotillin/HflK/C (SPFH) superfamily of proteins is a very diverse family of prokaryotic and eukaryotic membrane proteins that carry a conserved N-terminal domain called the SPFH domain (Hinderhofer et al., 2009). Although it is still a matter of debate, SPFH proteins were proposed to have emerged independently in different kingdoms, suggesting their

important cellular functions (Rivera-Milla et al., 2006). SPFH proteins are arranged in nanodomains in the membranes of diverse subcellular compartments and are involved in various mechanisms related to membranes (Browman et al., 2007; Stoner et al., 2025). Among others, Stomatin, Mechanosensory protein-2, and Podocin play a role in the regulation of ion channels in animals (Huber et al., 2006; Price et al., 2004) and Flotillins (Flots) are implicated in specific endocytic mechanisms in both animal and plant cells (Glebov et al., 2006; Li, Liu, Wan, Chen, Wang, Mettbach, Baluska, et al., 2012). SPFH proteins have been proposed for a long time to act as scaffolding proteins in membrane nanodomains (Langhorst et al., 2005), although experimental evidence remains limited. Nevertheless, an interesting example is provided in plants by *Medicago truncatula* FLOT4 that acts as a central hub during primary nanodomain assembly by recruiting the remorin SYMREM1 that in turn interacts with and stabilizes the activated LYSINE MOTIF KINASE 3 (LYK3) receptor into nanodomains, insuring symbiotic root infection (Liang et al., 2018). How SPFH proteins assemble in nanodomains is not known, but this process may rely on their propensity to form large homo- and hetero-oligomers (Browman et al., 2007). Early observations by electron microscopy highlighted that mitochondrial prohibitins from yeast form ring-shaped structures (Tatsuta et al., 2005). Then, the structure of SPFH proteins from *Escherichia coli* named HflC and HflK revealed that these proteins assemble in a large circular complex composed of 12 copies of HflK–HflC dimers that delimits a laterally segregated membrane domain of 20 nm in diameter (Ma et al., 2022). This highlights the role of SPFH proteins in nanodomain structuration through a possible compartmentation of lipids and proteins. So far, the domains involved in the oligomerization of SPFH proteins were mostly identified in their C-terminal parts, such as for animal and plant Flot, in the so-called Flot domain, and for human Stomatin (Singh et al., 2022; Solis et al., 2007; Umlauf et al., 2006; Yu et al., 2017). However, the structure of the HflK–HflC multimer from *E. coli* revealed complex and multiple interactions between monomers also through their SPFH domains (Ma et al., 2022).

Plants possess a specific group of SPFH proteins named hypersensitive induced reaction (HIR) proteins composed of four members in *Arabidopsis thaliana* (HIR1–HIR4). HIR contribute to immunity against various pathogens such as bacteria, viruses and fungi in several plant species (Li et al., 2019; Liu, Zhao, et al., 2024; Mei et al., 2020; Qi et al., 2011). Interestingly, HIR interact with proteins implicated in the response to pathogens, reinforcing the link between HIR and plant immunity (Hdedeh et al., 2025; Jung & Hwang, 2007; Qi et al., 2011; Qi & Katagiri, 2012; Zhou et al., 2009). Although the underlying molecular mechanisms involving HIR proteins remain enigmatic, HIR are implicated in the reactive oxygen species (ROS) burst occurring in response to the bacterial peptide flg22 (Liu, Zhao, et al., 2024). HIR proteins do not contain transmembrane domains, but are associated with membranes (Danek et al., 2016). Except HIR3, all the Arabidopsis HIR proteins arrange in nanodomains in the PM and display low lateral mobility dictated in part by the cell wall (Danek et al., 2020). In animal cells, Flot2 association with membranes is ensured by *N*-myristoylation and S-acylation (Neumann-Giesen et al., 2004). *N*-myristoylation and S-acylation are post-translational lipidation modifications of target proteins that consist in the addition of a myristate to a N-terminal glycine through an amide bond and the addition of a fatty acyl group, usually palmitate or stearate, to cysteine residues via a thioester bond, respectively (Hemsley, 2015). When a palmitate is linked to a protein, S-acylation can be referred to as palmitoylation. Note that S-acylation was historically known as palmitoylation. *N*-myristoylation and S-acylation are well known to provide hydrophobic anchors allowing the association of proteins to membranes in plant cells (Hemsley, 2015; Liu, Qu, et al., 2024; Lopez Vazquez et al., 2023). The S-acylation of some *A. thaliana* and *M. truncatula* remorins contributes to their PM association but is not responsible for their arrangement in nanodomains (Konrad et al., 2014). S-acylation function is not restricted to membrane association since it can be also implicated in the formation and stabilization of protein complexes (Hurst et al., 2023; Lakkaraju et al., 2012). Interestingly, Arabidopsis HIR proteins were shown to be *N*-myristoylated and S-acylated (Hemsley et al., 2013; Kumar et al., 2022; Majeran et al., 2018). Similarly to other SPFH proteins, HIR are able to homo- and hetero-oligomerize (Liu, Zhao, et al., 2024; Qi et al., 2011). However, it is not known whether the oligomerization plays a role in the recruitment of HIR into membrane nanodomains or in the organization of the domains themselves.

In plants, the lipid composition of the PM influences the dynamics of proteins and their organization into nanodomains (Gronnier et al., 2018; Jaillais & Ott, 2020). Among lipids, the role of sterols was probably the most explored since sterols, together with sphingolipids, were historically described to be important for nanodomain organization by forming liquid ordered domains in the PM (Grosjean et al., 2015; Mamode Cassim et al., 2019). Arabidopsis plants treated with the sterol-depleting agent methyl-β-cyclodextrin (mβCD) or the sterol biosynthesis mutant *cyclopropylsterol isomerase 1* (*cpi1-1*) both display altered intracellular dynamics of Flot1 (Cao et al., 2020; Li, Liu, Wan, Chen, Wang, Mettbach, Baluska, et al., 2012).

Interestingly, both sterols and phosphatidylinositol 4-phosphate are required for the nanodomain organization of *Solanum tuberosum* StREM1;3 in the PM (Gronnier et al., 2017). Phosphatidylserine (PS) is required to stabilize the GTPase Rho-of-Plant 6 (ROP6) in PM nanodomains (Platre et al., 2019). Interestingly, PS and sphingolipids that are both closely linked to the organization of PM nanodomains in plants display a common trait, a very long chain fatty acid (VLCFA) that corresponds to fatty acids with more than 18 carbon atoms. These data illustrate that one lipid category can influence the patterning in the PM of functionally unrelated proteins and that multiple lipid species can be required for the proper organization in the PM of a given protein.

Although SPFH proteins were identified more than 25 years ago, their function and regulation remain largely unknown in plants. Here, we sought to better understand the mechanisms governing the PM targeting and the organization into nanodomains of the plant-specific HIR proteins, using Arabidopsis HIR2 isoform as a model. We highlighted that the mono S-acylation of HIR2 either on cysteine 6 or on cysteine 7 is mandatory for its PM localization in Arabidopsis. Combining state-of-the-art microscopy techniques, we showed that: (i) the lipid composition in sterols and VLCFA of the PM influences the organization of HIR2 into nanodomains and HIR2 molecule dynamics, (ii) HIR2 nano-organization in the PM is driven by HIR2 oligomerization through its C-terminal part. In addition, we provided evidence that the nanodomain organization of HIR2 is required to stimulate the ROS burst in plant cells in response to flg22.

RESULTS

HIR2 and remorins do not co-localize in PM nanodomains

To investigate HIR2 intracellular dynamics, we generated Arabidopsis transgenic lines expressing HIR2 fused to the fluorescent protein mCherry, under the control of *HIR2* promoter. In the root, *HIR2* promoter drives HIR2-mCherry expression specifically in epidermal cells, in root hairs as well as in the lateral root cap (Figure S1). HIR2-mCherry fluorescence was also observed in hypocotyl cells and in cotyledon pavement cells. At the subcellular level, whatever the imaged tissue, HIR2-mCherry protein was only localized in the PM (Figure S1), in accordance with previous works (Danek et al., 2020; Qi et al., 2011). We verified the expression of HIR2-mCherry fusion protein in Arabidopsis transgenic lines via an anti-mCherry immunoblot. We observed a strong signal at the expected molecular weight of HIR2-mCherry as well as a faint signal of higher molecular weight, both of which being not observed in protein extracts from wild-type (WT) plants, showing the specificity of these signals (Figure S2). Similar signals were detected when HIR2-mCherry was transiently expressed under the control of *HIR2* promoter in *Nicotiana benthamiana* leaves, whereas no signal was detected in uninfiltrated leaves (Figure S2).

Remorins are abundant PM proteins that are probably the most studied proteins arranging into nanodomains in plants (Gronnier et al., 2017; Jarsch et al., 2014; Raffaele et al., 2009). We investigated the level of co-localization between two remorins from *A. thaliana*, REM1.2 and REM1.3, fused to the YFP (Jarsch et al., 2014), and HIR2-mCherry, the three proteins being expressed under the control of their respective endogenous promoters in Arabidopsis. Spinning-disk microscopy analysis performed on root epidermal cells revealed a very weak co-localization between the two remorins and HIR2 in PM nanodomains (Figure 1A,B), demonstrated by low Pearson's correlation coefficients (PCC) (Figure 1C).

HIR2 is mono S-acylated on either C6 or C7, which ensures its PM localization

To determine how HIR proteins, that do not contain transmembrane domains, are targeted to and associate with the PM, we investigated the role of lipidations. Indeed, all four HIR isoforms were found to be N-terminally *N*-myristoylated on glycine 2 (Majeran et al., 2018). To verify that the HIR2-mCherry fusion protein used in this study was indeed *N*-myristoylated, we immunopurified HIR2-mCherry expressed under the control of the *HIR2* promoter in Arabidopsis seedlings and then analyzed HIR2-mCherry by LC–MS/MS (Figure S3). We observed that the N-terminus of the HIR2-mCherry fusion protein exhibited a truncation of the initiating methionine and *N*-myristoylation of the exposed glycine. Since no other form of the N-terminal tail could be detected, we assume that 100% of the cellular pool of HIR2-mCherry is indeed *N*-myristoylated on G2. In addition to being *N*-myristoylated, HIR proteins are S-acylated (Hemsley et al., 2013). Predictions using GPS-Palm (Ning et al., 2021) suggested that in HIR2, C6 and C7 could be the palmitoylation sites (Figure 2U). An atlas of Arabidopsis protein S-acylation suggested that C58 in HIR2 was also S-acylated (Kumar et al., 2022). To study the role of *N*-myristoylation and S-acylation in HIR2 dynamics, amino acids G2, C6, C7, and C58 were mutated to alanine, individually or in combinations. WT and mutated HIR2 proteins fused to mCherry were transiently expressed in *N. benthamiana* leaf epidermal cells under the control of the *HIR2* promoter (Figure 2A–J; Figure S4). Confocal microscopy analysis revealed that the individual mutations G2A, C6A, C7A, and C58A did not alter HIR2 PM localization (Figure 2B–E). By contrast, the C6A, C7A double mutation induced a strong intracellular retention of HIR2 protein (Figure 2F). A similar mis-localization was observed for $HIR2^{G2A,C6A,C7A}$ or $HIR2^{C6A,C7A,C58A}$ mutated proteins

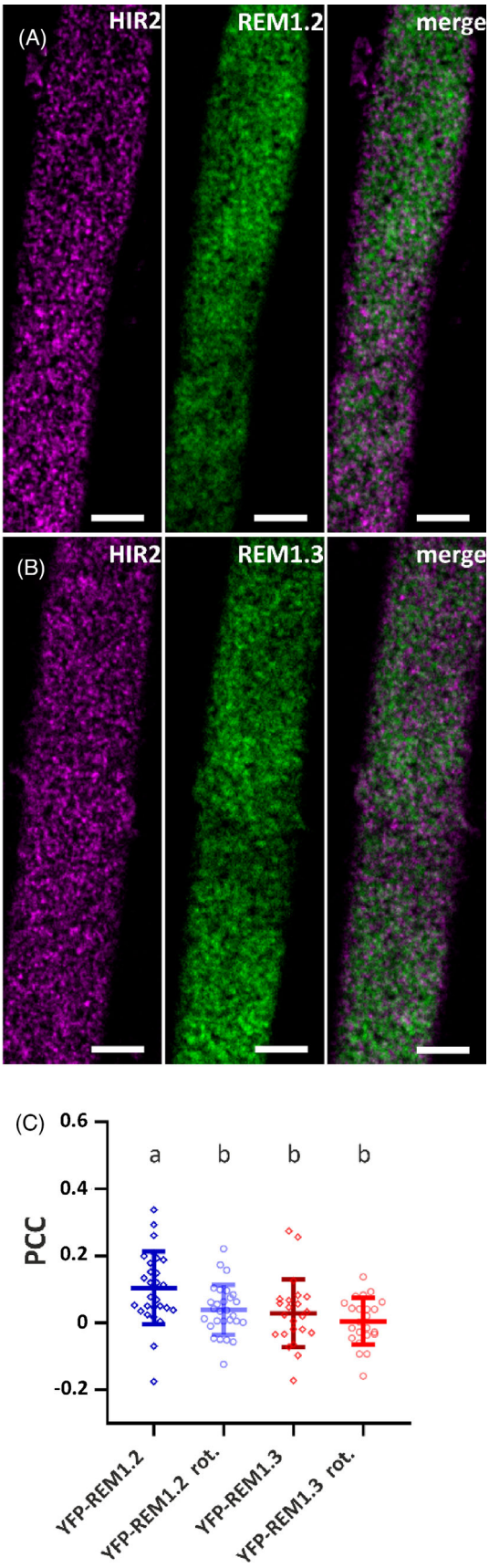

Figure 1. HIR2 and remorins do not co-localize in plasma membrane (PM) nanodomains.
Spinning-disk microscopy analyses of root epidermal cells from pHIR2::HIR2-mCherry Arabidopsis transgenic lines co-expressing pREM1.2::YFP-REM1.2 (A) or pREM1.3::YFP-REM1.3 (B). In the majority, in (A) and (B), HIR2-mCherry PM nanodomains (left panels) and YFP-REM PM nanodomains (middle panel) do not co-localize (merge, right panel). Arabidopsis seedlings were grown for 11 days on MS/2 medium. Scale bars: 5 μm.
(C) Quantification of the co-localization in PM nanodomains between HIR2-mCherry and YFP-REM1.2/YFP-REM1.3 proteins using Pearson's correlation coefficient (PCC). Square regions of interest were analyzed. As a control for random co-localization, the same regions where the YFP channel was rotated by 90° with respect to the mCherry channel were analyzed (rot.). For each co-localization test, 23–28 cells were analyzed. Scatter plots with indicated mean ± standard deviation. Letters indicate significant differences ($P < 0.05$, one-way ANOVA with *post-hoc* Tukey–Kramer multiple comparison test).

(Figure 2G,J). On the other hand, when the C58A mutation was combined with either the C6A or C7A mutations, $HIR2^{C6A,C58A}$ and $HIR2^{C7A,C58A}$ proteins were still localized at the PM (Figure 2H,I). Similar subcellular localizations were observed when WT and mutated HIR2 proteins fused to mCherry were stably expressed in Arabidopsis (Figure 2K–T). Notably, the double mutation C6A, C7A induced an intracellular mis-localization of HIR2 in root epidermal cells (Figure 2P). Altogether, these results suggest that: (i) *N*-myristoylation is not required for HIR2 PM targeting, (ii) C58 probably does not play a role in HIR2 PM localization, (iii) C6 and C7 together are essential to address HIR2 to the PM.

To analyze the role of S-acylation in HIR2 PM localization, we first used the S-acylation inhibitor 2-bromopalmitate (2-BP) (Zhang et al., 2015). Although in mock-treated Arabidopsis seedlings HIR2-mCherry protein was only detected in the PM of root epidermal cells, 2-BP treatment induced a strong intracellular mis-localization of HIR2-mCherry (Figure 3A, right). The subcellular localization of the PM protein GFP-LTi6b, which is not S-acylated, remained largely unchanged under 2-BP treatment, showing the specificity of 2-BP in this experiment. These results suggest that S-acylation is required for the localization of HIR2 in the PM in Arabidopsis cells.

Then, we analyzed the impact of C6A and C7A mutations on HIR2 S-acylation and also investigated the effect of G2A mutation, since *N*-myristoylation can be a prerequisite for S-acylation (Ueda et al., 2001). To do so, we performed a polyethylene glycol (PEG)-shift assay on Arabidopsis seedlings expressing WT HIR2 protein and HIR2 mutants fused to mCherry. The PEG-shift assay allows us to selectively replace S-fatty acids with maleimide-functionalized polyethylene glycol (mPEG-Mal) of defined mass, which induces a mobility shift of the protein proportional to the number of S-fatty acylated cysteines (Kumar et al., 2022; Percher et al., 2017). Here, we adapted the protocol described by Percher et al. (2017).

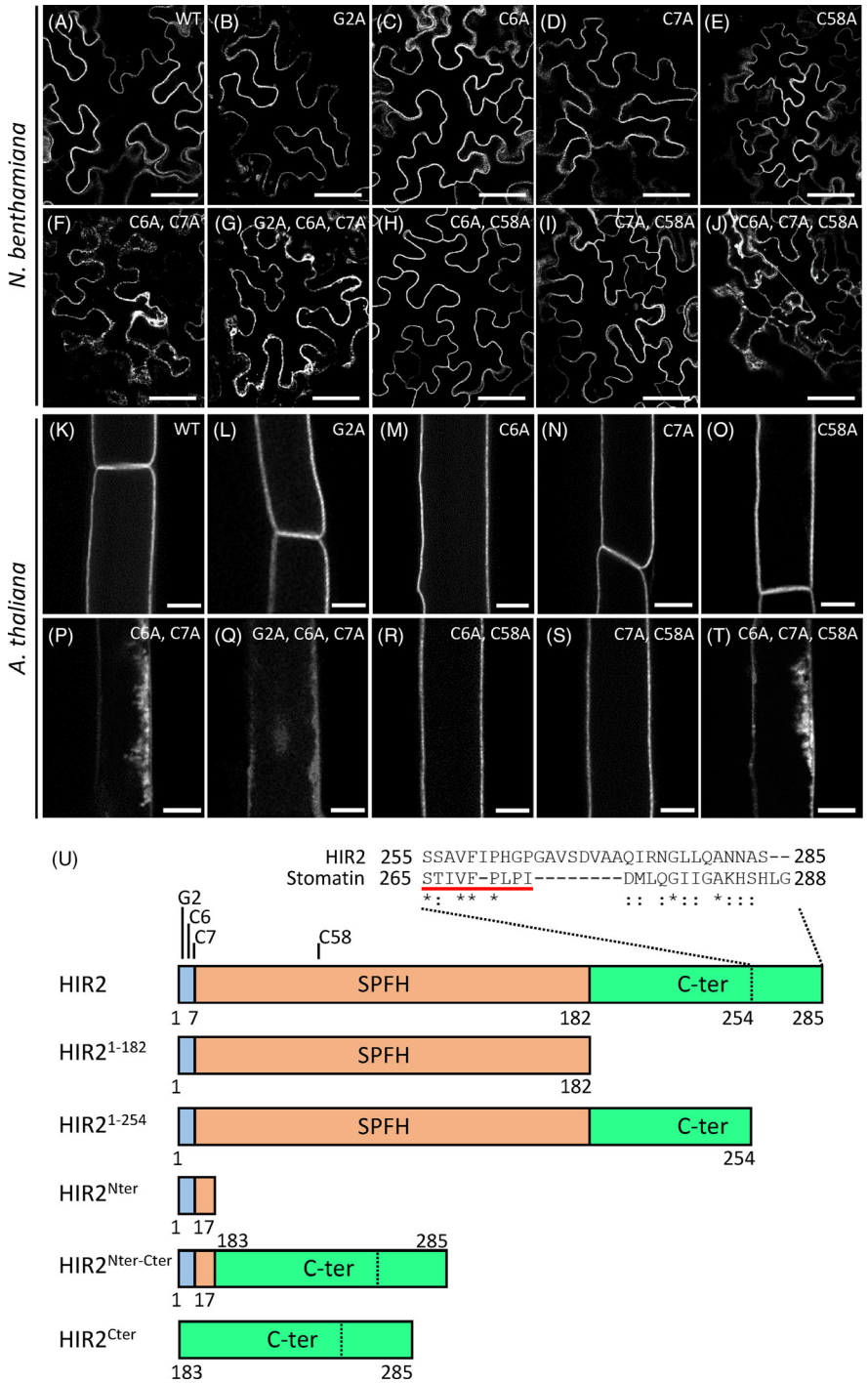

Figure 2. Simultaneous mutations of C6 and C7 induce HIR2 intracellular retention in plant cells.
The subcellular localization of HIR2 point mutants fused to mCherry and expressed under the control of *HIR2* promoter in *Nicotiana benthamiana* leaf epidermal cells (A–J) and in the root epidermal cells of Arabidopsis transgenic lines (K–T) was analyzed by scanning confocal microscopy. (A, K) HIR2-mCherry. (B, L) $HIR2^{G2A}$-mCherry. (C, M) $HIR2^{C6A}$-mCherry. (D, N) $HIR2^{C7A}$-mCherry. (E, O) $HIR2^{C58A}$-mCherry. (F, P) $HIR2^{C6A,C7A}$-mCherry. (G, Q) $HIR2^{G2A,C6A,C7A}$-mCherry. (H, R) $HIR2^{C6A,C58A}$-mCherry. (I, S) $HIR2^{C7A,C58A}$-mCherry. (J, T) $HIR2^{C6A,C7A,C58A}$-mCherry. Secant views are shown. Arabidopsis plantlets were grown 11 days on MS/2 medium. Scale bars represent 50 and 10 μm in panels (A–J) and (K–T), respectively.
(U) Schematic representation of HIR2 protein and the variants used in this work. HIR2 protein contains a N-terminal sequence composed of seven amino acids, a SPFH domain (position 8–182) that was defined according to the Pfam website and a C-terminal domain (position 183–285). A sequence present in the very C-terminus of HIR2 displays homology to an oligomerization motif found in human Stomatin (underlined in red). Glycine 2 (G2) was shown to be *N*-myristoylated, cysteine 58 (C58) was proposed to be S-acylated and cysteines 6 and 7 (C6, C7) were predicted to be S-acylation sites according to GPS-Palm. Truncated variants of HIR2 and chimeric proteins are represented. * indicates a conserved residue, : indicates strongly similar residues.

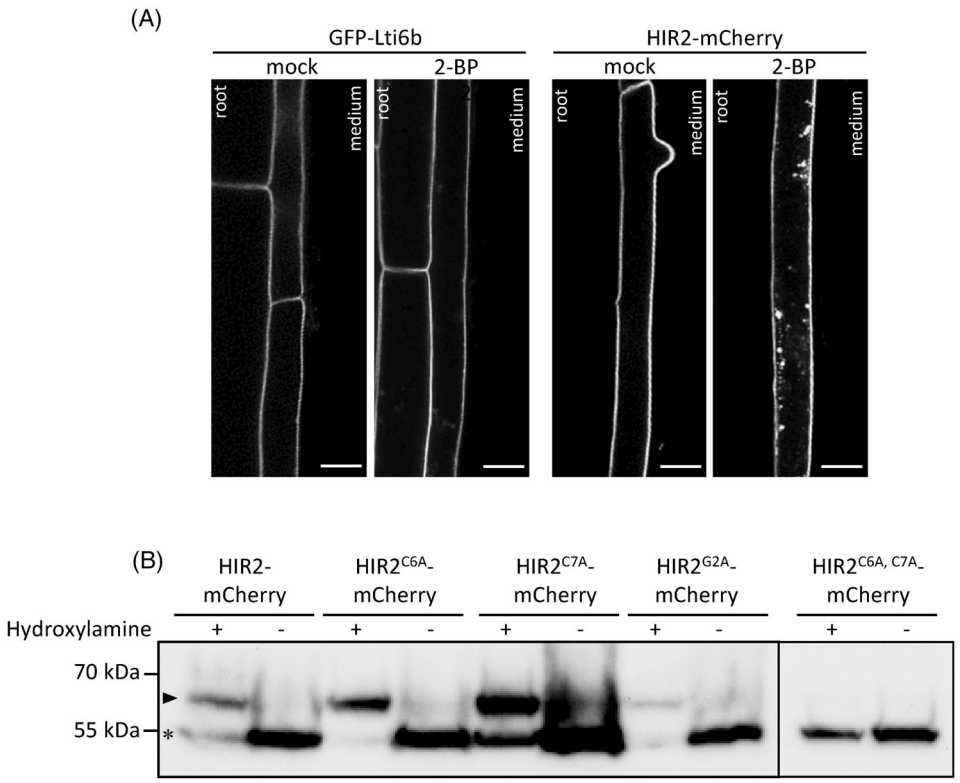

Figure 3. Mono S-acylation is required for HIR2 plasma membrane (PM) localization.
(A) Inhibition of S-acylation using 2-bromopalmitate (2-BP) disturbs HIR2 subcellular localization. The subcellular localization of HIR2-mCherry and GFP-LTi6b (control) expressed under the control of *HIR2* and *35S* promoters, respectively, was analyzed by scanning confocal microscopy in the roots of 11-day-old Arabidopsis seedlings treated with 2-BP or mock-treated (mock). Scale bars represent 20 μm.
(B) HIR2 is mono S-acylated, and simultaneous mutations of C6 and C7 abolish HIR2 S-acylation. The S-acylation of WT HIR2, HIR2^{C6A}, HIR2^{C7A}, HIR2^{G2A}, and HIR2^{C6A,C7A} proteins fused to the mCherry and expressed under the control of *HIR2* promoter in Arabidopsis transgenic lines was assessed with a PEG-shift assay combined with anti-mCherry immunoblots. Following the cleavage of S-acyl groups with the thioester cleavage reagent hydroxylamine, a maleimide-functionalized polyethylene glycol (mPEG-Mal) was selectively coupled to free cysteines, which induced a mobility shift for each S-acylation site. In the absence of hydroxylamine (−), no mass shift should be observed with a signal at approximately 55 kDa, corresponding to the expected molecular weight of HIR2 and HIR2 mutated proteins fused to the mCherry. The S-acylated form of WT HIR2, but also some HIR2 mutated proteins fused to the mCherry, is indicated by the detection of a signal at approximately 65 kDa in the presence of hydroxylamine (+). Non-S-acylated and S-acylated HIR2 and HIR2 mutated proteins fused to the mCherry are indicated by a star and an arrowhead, respectively. Arabidopsis seedlings were grown for 11 days on MS/2 medium. *corresponds to non-S-acylated HIR2 proteins.

Briefly, following protein disulfide bond reduction and capping of non-modified cysteines with N-ethylmaleimide (NEM), cysteine-coupled fatty acid groups were specifically cleaved with hydroxylamine, followed by the coupling of 5 kDa mPEG-Mal. To control the efficiency of the capping of unmodified cysteines by NEM, an experiment was also performed in the absence of hydroxylamine (−Hyd). An anti-mCherry immunoblot revealed the presence of a single signal at the expected molecular weight for HIR2-mCherry (~55 kDa) in −Hyd condition, whereas in the presence of hydroxylamine (+Hyd) a single mass shift was observed for HIR2-mCherry (~65 kDa) (Figure 3B; Figure S5). By contrast, no mass shift was observed for the HIR2^{C6A,C7A}-mCherry mutated protein in +Hyd condition, showing that C6A, C7A double mutation abolished HIR2 S-acylation. For both HIR2^{C6A}-mCherry and HIR2^{C7A}-mCherry, a single mass shift similar to the one observed for HIR2-mCherry was detected in +Hyd condition, suggesting that these two mutated proteins are still S-acylated (Figure 3B; Figure S5). Since WT HIR2, HIR2^{C6A} and HIR2^{C7A} displayed the same S-acylation profile whereas HIR2^{C6A,C7A} was not S-acylated, these data strongly suggest that HIR2 is mainly mono S-acylated on either C6 or C7. Note that for HIR2-mCherry in +Hyd condition, a very faint signal was also observed above the intense signal at ~65 kDa, suggesting that a minor population of HIR2 may be di-S-acylated. In +Hyd condition, a mass shift similar to the WT (~65 kDa) was observed for HIR2^{G2A}-mCherry, showing that G2A mutation does not interfere with HIR2 S-acylation. Note that for HIR2, HIR2^{C6A}, HIR2^{C7A}, and HIR2^{G2A} fusion proteins, a signal was also detected in +Hyd at ~55 kDa, which could indicate that not all the protein pools are S-acylated,

but may also result from an incomplete binding of mPEG-Mal during the PEG-shift assay. The absence of mass shift for HIR2^{C6A,C7A} in +Hyd condition highly suggests, since C58 is not mutated in this protein, that C58 is not S-acylated in our experimental conditions or that it requires prior S-acylation on C6 or C7.

HIR2 PM targeting likely relies on mechanisms independent of the secretory pathway

To explore the localization of the intracellularly retained HIR2^{C6A,C7A} protein, we performed cell fractionation on *N. benthamiana* leaf tissues expressing HIR2^{C6A,C7A}-mCherry. Surprisingly, similarly to WT HIR2, HIR2^{C6A,C7A} protein was exclusively detected in the microsomal fraction that corresponds to membranes and not in the cytosolic fraction (Figure S6). Identical results were obtained for HIR2^{G2A}, HIR2^{C6A}, HIR2^{C7A}, and HIR2^{G2A,C6A,C7A} proteins. This suggests that lipidations are not the sole way to anchor HIR2 into membranes. We hypothesized that HIR2^{C6A,C7A} protein may be retained in an intermediate compartment *en route* to the PM, possibly the ER. However, no clear co-localization was observed between HIR2^{C6A,C7A}-mCherry and the pHluorine-HDEL ER marker in *N. benthamiana* leaf epidermal cells, and a low PCC was measured (Figure S7A–D). In plants, the majority of PM localized proteins exit the ER through the action of the coat protein complex II (COPII) machinery and then traffic along the secretory pathway to ultimately reach the PM (Chung et al., 2016). To investigate whether HIR2 PM delivery requires the COPII-mediated pathway, we used a dominant-negative (DN) version of the COPII component SAR1 protein that is essential to initiate COPII vesicle budding (daSilva et al., 2004). As a positive control to monitor the effect of SAR1-DN, we used the Arabidopsis proton pump H^+-ATPase2 (AHA2) that is mainly localized in the PM when expressed alone in *N. benthamiana* leaf epidermal cells (Figure S7E,F) (Lefebvre et al., 2004). Upon co-expression with SAR1-DN-YFP, AHA2-mCherry was fully retained in the ER, whereas HIR2-mCherry trafficking/delivery to the PM was only slightly disturbed, suggesting that HIR2 targeting to the PM mainly occurs independently of COPII vesicles (Figure S7I–L).

To try to identify the intracellular compartment containing HIR2^{C6A,C7A} protein, we performed co-localization analysis in *N. benthamiana* leaf epidermal cells using endomembrane markers. As a positive control, we co-expressed HIR2^{C6A,C7A}-mEGFP and HIR2^{C6A,C7A}-mCherry and measured a very high PCC (Figure S8A,G). When co-expressing HIR2^{C6A,C7A}-mEGFP or HIR2^{C6A,C7A}-mCherry with Rhal-RFP (late endosome/pre-vacuolar compartment), ST-RFP (Golgi), VHAa1-RFP (trans-Golgi network/early endosome) and GFP-SYP61 (trans-Golgi network/early endosome), no co-localization was observed (Figure S8B–E), as attested by low PCC values that were not significantly different from the negative control (Rhal + SYP61) (Figure S8F,G). Therefore, the nature of the compartment in which HIR2^{C6A,C7A} is retained remains unknown.

G2A, C6A, C7A, and C58A single mutations do not affect HIR2 PM nanodomain organization

Although G2A, C6A, and C7A mutations did not affect HIR2 PM targeting, we wondered whether they could interfere with HIR2 nanodomain formation. To investigate HIR2 clustering, we used total internal reflection fluorescence (TIRF) microscopy that displays an enhanced signal-to-noise ratio due to shallow excitation of the cells compared with other microscopy techniques and constitutes one of the state-of-the-art microscopy techniques to study nanodomain organization in the PM (Platre et al., 2019; Smokvarska et al., 2020). Importantly, we did not perform any imaging post-processing that can sometimes produce nanodomain-resembling artifacts (Jaillais & Ott, 2020). When expressed in *N. benthamiana* leaf epidermal cells or in Arabidopsis root epidermal cells, HIR2^{G2A}, HIR2^{C6A}, and HIR2^{C7A} mutated proteins fused to mCherry displayed a dotty-like pattern in the PM, characteristic of nanodomain-organized proteins that was similar to the pattern of HIR2-mCherry (Figure 4A–D,H–K). To quantify the level of clustering of WT HIR2 and mutated HIR2 proteins in the PM, the coefficients of variance (CV) of pixel intensity, that reflect here the heterogeneity of protein distribution in the PM, were calculated from TIRF acquisitions (Danek et al., 2020; Gronnier et al., 2017; Retzer et al., 2017). CV values for WT HIR2, HIR2^{G2A}, HIR2^{C6A}, and HIR2^{C7A} proteins were not significantly different (Figure 4O). Therefore, we concluded that: (i) *N*-myristoylation is not involved in HIR2 nanodomain organization, (ii) single S-acylation mutants display a normal arrangement into nanodomains likely due to the interchangeability of S-acylation sites, C6 or C7. Although the PEG-shift assay highly suggested that C58 is not S-acylated in our experimental conditions, we also tested the clustering of HIR2^{C58A}, HIR2^{C6A,C58A}, and HIR2^{C7A,C58A} mutated proteins. TIRF analysis revealed that all these mutated proteins displayed a normal arrangement into PM nanodomains (Figure 4E–G,L–O), showing that C58 residue has no role in HIR2 nano-organization, nor in its PM localization as mentioned above.

Sterols and VLCFA influence HIR2 organization in the PM

To investigate the importance of PM lipid composition on HIR2 nanodomain organization, we focused our attention on: (i) sterols that play a crucial role in the structuration of nanodomains, (ii) VLCFA, since PS and sphingolipids, which both contain VLCFA, are closely linked to the organization of nanodomains (Gronnier et al., 2017; Grosjean et al., 2015; Platre et al., 2019). First, we used the sterol synthesis inhibitor fenpropimorph (FEN) that alters the PM sterol composition but not the total amount of sterols (Gronnier et al., 2017).

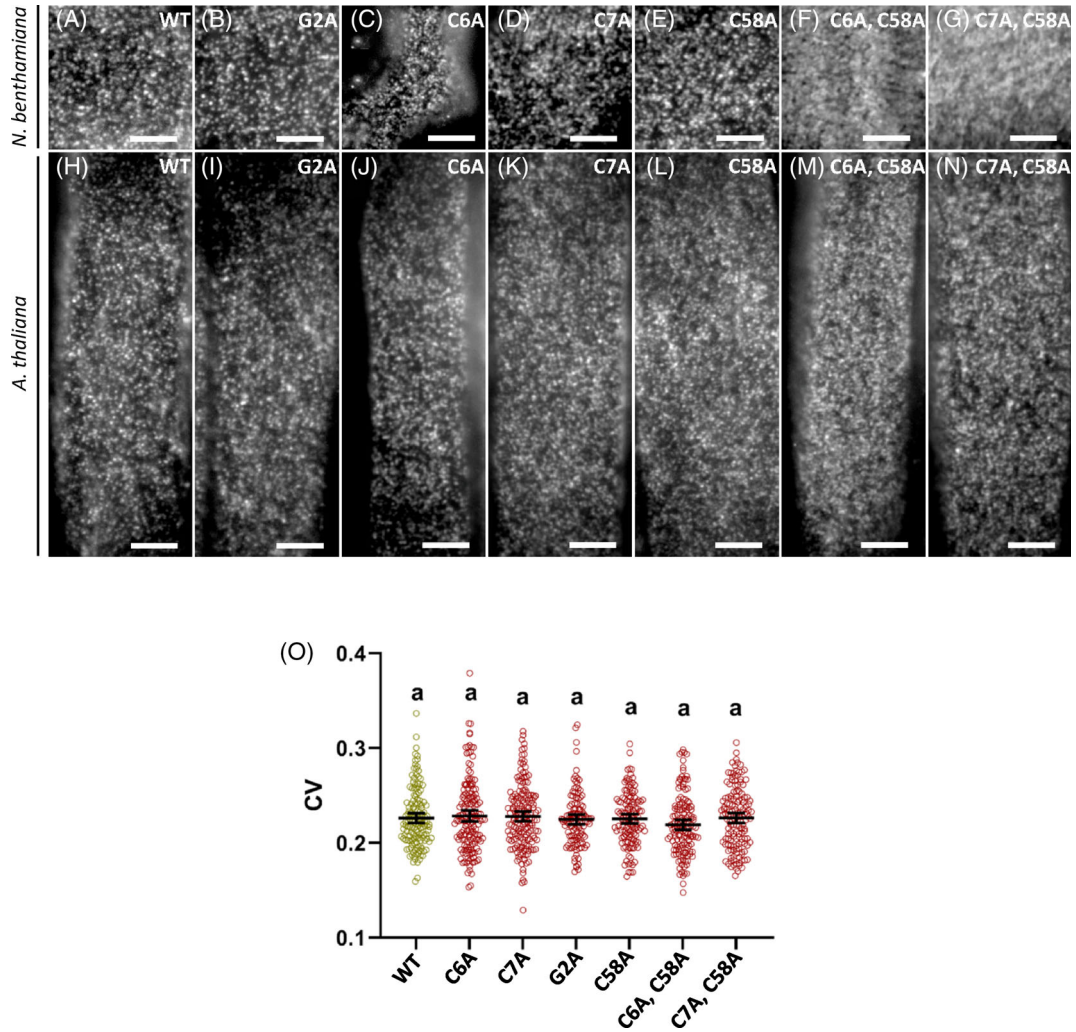

Figure 4. G2A, C6A, C7A, and C58A single mutations do not affect HIR2 plasma membrane (PM) nanodomain organization.
Total internal reflection fluorescence (TIRF) microscopy analysis was performed on the PM of *Nicotiana benthamiana* leaf epidermal cells (A–G) or *Arabidopsis thaliana* root epidermal cells (H–O) expressing HIR2 point mutants fused to mCherry and expressed under the control of the *HIR2* promoter. Note that the arrangement in nanodomains was only investigated for HIR2 mutated proteins that are still targeted/localized to the PM. (A, H) HIR2-mCherry. (B, I) $HIR2^{G2A}$-mCherry. (C, J) $HIR2^{C6A}$-mCherry. (D, K) $HIR2^{C7A}$-mCherry. (E, L) $HIR2^{C58A}$-mCherry. (F, M) $HIR2^{C6A,C58A}$-mCherry. (G, N) $HIR2^{C7A,C58A}$-mCherry.
(O) Coefficients of variance (CV) of fluorescence intensity were calculated from TIRF experiments performed as in (H) to (N) on Arabidopsis root epidermal cells. Error bars correspond to a confidence interval at 95%. For each protein, between 125 and 175 intensity profiles from more than 25 cells from three independent biological replicates were analyzed. Letters indicate significant differences (*P*-value <0.05, one-way ANOVA with *post-hoc* Tukey multiple comparison test). Arabidopsis plantlets were grown 7 days on MS/2 medium. Scale bars represent 5 μm.

Following FEN treatment, HIR2-mCherry clustering was decreased in the PM of Arabidopsis root epidermal cells compared with non-treated or mock-treated plants (Figure 5A–C), resulting in a reduction of the CV value (Figure 5E). A similar effect of FEN was observed on the nanodomain organization of GFP-StREM1.3, as previously reported (Figure S9) (Gronnier et al., 2017). Second, to alter the composition of VLCFA incorporated in the pool of sphingolipids and PS in the PM, we used metazachlor (MTZ) that reduces the length of the chains of VLCFA by targeting the 3-ketoacyl CoA synthase enzymes (Wattelet-Boyer et al., 2016). MTZ treatment dramatically changed the localization of HIR2-mCherry that displayed a homogeneous signal in the PM of Arabidopsis root epidermal cells (Figure 5D), different from the controls where HIR2-mCherry was clustered (Figure 5A,B), which was accompanied by a strong reduction of the CV value (Figure 5E). To ensure that MTZ treatment did not induce a general disorganization of the PM, we showed that the nanodomain organization of GFP-StREM1.3 expressed in Arabidopsis root epidermal cells was not affected by MTZ (Figure S10). Altogether, these results showed that both sterols and VLCFA are important for the nanodomain organization of HIR2 in the PM.

To analyze deeper the effect of the disruption of the sterol and VLCFA composition on HIR2 dynamics in the

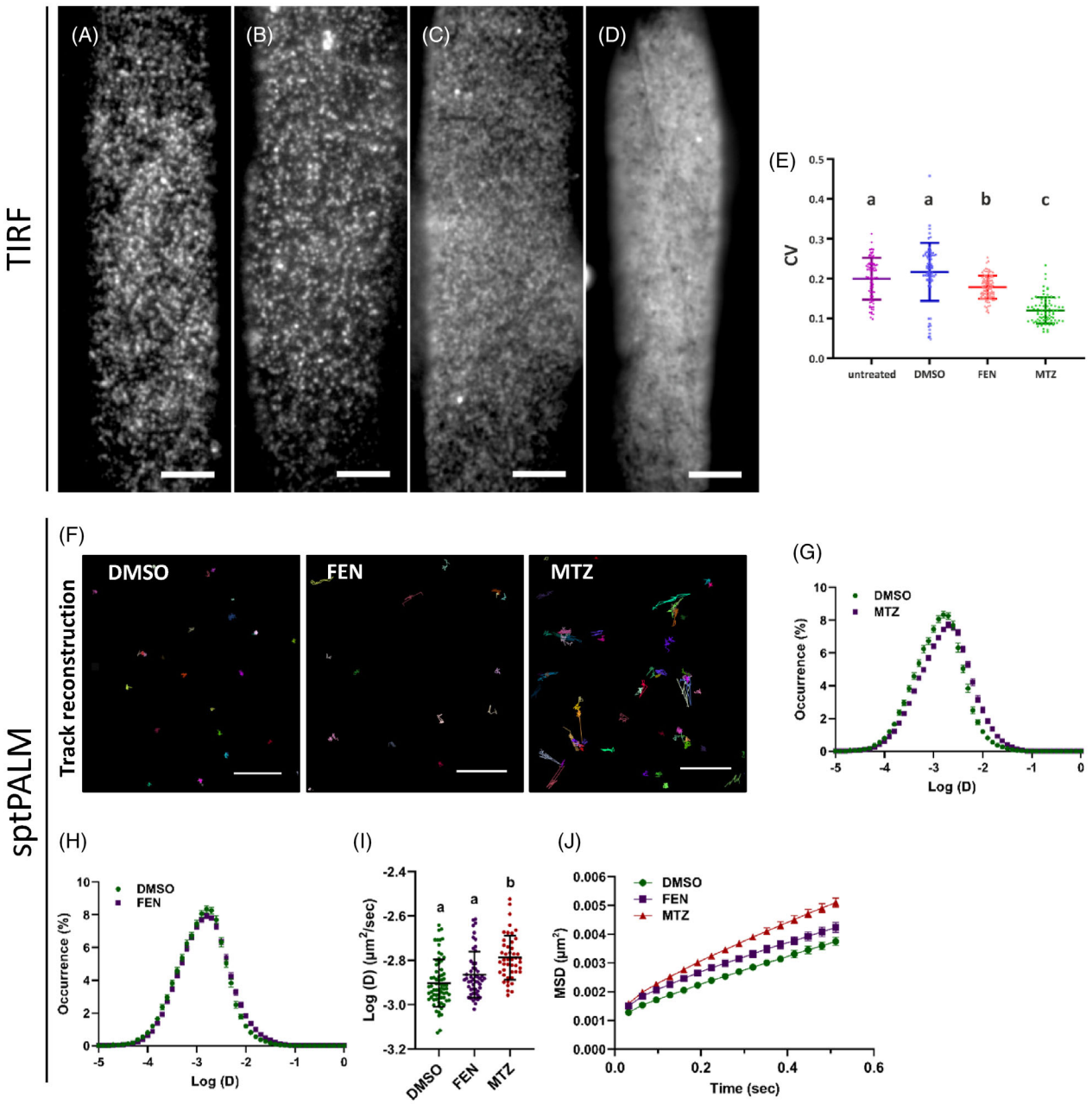

Figure 5. Sterols and very long chain fatty acids (VLCFA) are involved in the organization of HIR2 in the plasma membrane (PM).
Total internal reflection fluorescence (TIRF) microscopy analysis on the PM of root epidermal cells from pHIR2::HIR2-mCherry transgenic Arabidopsis seedlings, non-treated (A), mock-treated with DMSO (B), treated with fenpropimorph (FEN) (C) or metazachlor (MTZ) (D). Scale bars represent 5 µm.
(E) Coefficient of variance (CV) of fluorescence intensity determined from TIRF images of root epidermal cells expressing HIR2-mCherry and treated as in (A–D). Scatter plots with indicated mean ± standard deviation. For each treatment, between 70 and 100 intensity profiles from 20 cells were analyzed. Letters indicate significant differences ($P < 0.05$, one-way ANOVA with *post-hoc* Tukey–Kramer multiple comparison test).
(F–J) Single-particle-tracking photoactivated localization microscopy (sptPALM) was performed on the PM of root epidermal cells from pHIR2::HIR2-mEOS2 mock-treated Arabidopsis seedlings (DMSO) or seedlings treated with FEN or MTZ. (F) For each treatment, image reconstructions of several tens of single HIR2-mEOS2 molecule trajectories are indicated by different colors. Scale bars represent 10 µm. The distribution of HIR2-mEOS2 molecule instantaneous diffusion coefficient (D) (expressed in log [μm^2 sec^{-1}]) for the different treatments is presented in (G) and (H). (I) Quantification of the diffusion of HIR2-mEOS2 under the different treatments. For each treatment, between 50 and 60 cells from three independent biological replicates were analyzed. Letters indicate significant differences ($P < 0.05$, one-way ANOVA with *post-hoc* Tukey multiple comparison test). (J) Mean square displacement (MSD) curves of HIR2-mEOS2 molecules under the different treatments.

PM, we performed single-particle-tracking photoactivated localization microscopy (sptPALM) analysis, using an Arabidopsis transgenic line expressing HIR2 fused to mEOS2 photoconvertible fluorescent protein under the control of *HIR2* promoter. sptPALM is a super-resolution technique allowing us to visualize and track single molecules along time in living cells and measure different kinetic and organizational parameters including instantaneous diffusion (*D*) and mean square displacement (MSD) (Gronnier et al., 2017; Hosy et al., 2015; Martiniere et al., 2019). Upon mEOS2 stochastic photoactivation, sub-diffraction spots appeared with a blinking behavior, as expected from single molecules (Video S1). Typically, several thousand single HIR2-mEOS2 molecules were imaged from a single time series. The localization of molecules along time was retrieved and tracks were reconstructed with a spatial resolution of ~30 nm and a temporal resolution of 32 ms. Then, tracks were used to infer molecule instantaneous diffusion (Bayle et al., 2021) (Figure 5F–J). MTZ treatment increased the diffusion of HIR2-mEOS2 molecules in the PM of root epidermal cells ($D = 0.003 \pm 0.0001\ \mu m^2\ sec^{-1}$) compared with mock-treated conditions ($D = 0.002 \pm 0.0006\ \mu m^2\ sec^{-1}$) (Figure 5F,G,I). In addition, the MSD of HIR2-mEOS2 was faster in the presence of MTZ, showing an increased mobility of HIR2-mEOS2 molecules in the PM (Figure 5J). By contrast, FEN treatment induced a very slight but not significant increase of D and MSD parameters, showing that HIR2-mEOS2 diffusion was not affected by FEN (Figure 5F,H–J).

All of these data strongly suggest that both sterols and VLCFA influence HIR2 nano-organization in the PM, although with a different magnitude.

The C-terminal domain of HIR2 is required for its oligomerization

Since HIR2 protein is known to homooligomerize (Qi et al., 2011), we analyzed the effect of the co-expression of WT HIR2 protein with the $HIR2^{C6A,C7A}$ mutant that is retained intracellularly. Interestingly, upon co-expression with HIR2-mEGFP, $HIR2^{C6A,C7A}$-mCherry was relocalized from intracellular compartments to the PM (Figure S11A). In addition, HIR2-mEGFP and $HIR2^{C6A,C7A}$-mCherry proteins were strongly co-localized in clusters at the PM (Figure S11B,C). Therefore, the expression of WT HIR2 protein can drive non-acylated HIR2-mutated proteins to PM nanodomains.

We sought to identify the domains involved in HIR2 homooligomerization, this latter being probably important for HIR2 function. Interestingly, HIR2 protein carries in its very C-terminal part a sequence that displays a partial identity with an oligomerization motif present in the human SPFH protein Stomatin (Figure 2U) (Umlauf et al., 2006). We deleted this motif to generate the truncated $HIR2^{1-254}$ protein (amino acids 1–254) and also created the $HIR2^{1-182}$ truncated protein in which the whole C-terminal part was deleted to conserve the N-terminal sequence and the SPFH domain of HIR2 (amino acids 1–182) (Figure 2U). When expressed in *N. benthamiana* leaf epidermal cells and in Arabidopsis root epidermal cells, both $HIR2^{1-254}$ and $HIR2^{1-182}$ proteins fused to fluorophores were solely observed in the PM, as WT HIR2, showing that the C-terminal part of HIR2 is not required for PM targeting (Figure 6A–I). To analyze the effect of HIR2 C-terminal truncations on HIR2 oligomerization, we performed co-immunopurifications (co-IP) between HIR2, $HIR2^{1-254}$, $HIR2^{1-182}$ proteins fused to mEGFP and HIR2-Cherry expressed in *N. benthamiana*. HIR2-mCherry protein was co-purified with HIR2-mEGFP but not with $HIR2^{1-182}$-mEGFP (Figure 6J; Figure S12), showing that this truncated protein lost its capacity to interact with other HIR2 molecules. In addition, a faint mCherry signal was detected in $HIR2^{1-254}$-mEGFP IP fraction, indicating a weaker interaction between HIR2-mCherry and $HIR2^{1-254}$-mEGFP, compared with HIR2-mEGFP. To confirm the importance of the C-terminal domain of HIR2 in its homooligomerization, we performed Förster resonance energy transfer-fluorescence lifetime

Figure 6. The C-terminal part of HIR2 is required for oligomerization but not for plasma membrane targeting.
The subcellular localization of HIR2-mEGFP (A, D), $HIR2^{1-182}$-mEGFP (B, E) and $HIR2^{1-254}$-mEGFP (C, F) transiently expressed under the control of *HIR2* promoter in *Nicotiana benthamiana* leaf epidermal cells was analyzed by scanning confocal microscopy. $HIR2^{1-182}$ and $HIR2^{1-254}$ are truncated proteins corresponding to the first 182 and 254 amino acids of HIR2, respectively. (A–C) Secant views. (D–F) Maximum intensity projections constructed from *Z*-stack of 25 focal planes spanning from the epidermis surface to the positions shown in (A–C).
(G–I) Secant views of root epidermal cells from Arabidopsis transgenic lines expressing HIR2-mCherry (G), $HIR2^{1-182}$-mCherry (H) and $HIR2^{1-254}$-mEGFP (I) under the control of *HIR2* promoter. Scanning confocal microscopy, scale bars represent 50 μm. Arabidopsis plantlets were grown 11 days on MS/2 medium.
(J) Deletions in the C-terminal part of HIR2 disturb HIR2 oligomerization as revealed by co-immunopurifications. Immunopurifications (IP) using an anti-GFP antibody were performed on solubilized protein extracts from *N. benthamiana* leaves transiently co-expressing HIR2-mCherry with HIR2-mEGFP, $HIR2^{1-182}$-mEGFP or $HIR2^{1-254}$-mEGFP. Inputs and IP fractions were subjected to immunoblots (IB) with anti-GFP (top) and anti-mCherry antibodies (bottom).
(K–O) FRET-FLIM analyses were performed in *N. benthamiana* leaf epidermal cells expressing HIR2-mEGFP alone (K) or in combination with the following proteins: HIR2-mCherry (L), $HIR2^{1-182}$-mCherry (M), $HIR2^{1-254}$-mCherry (N) and MAP-mCherry (O), which served as a negative control for interaction. Scale bars represent 10 μm. mEGFP fluorescence lifetime is indicated by a color code from red for values of ≈3 ns to blue for values of ≈0.5 ns. (P) Graph showing the quantification of mEGFP fluorescence lifetime for the combinations shown in panels K–O. Scatter plots show the mean ± standard deviation. For each combination, 20 cells were analyzed. No significant differences were found ($P < 0.05$, one-way ANOVA with *post-hoc* Tukey–Kramer multiple comparison test). A representative experiment among three independent biological replicates is shown.

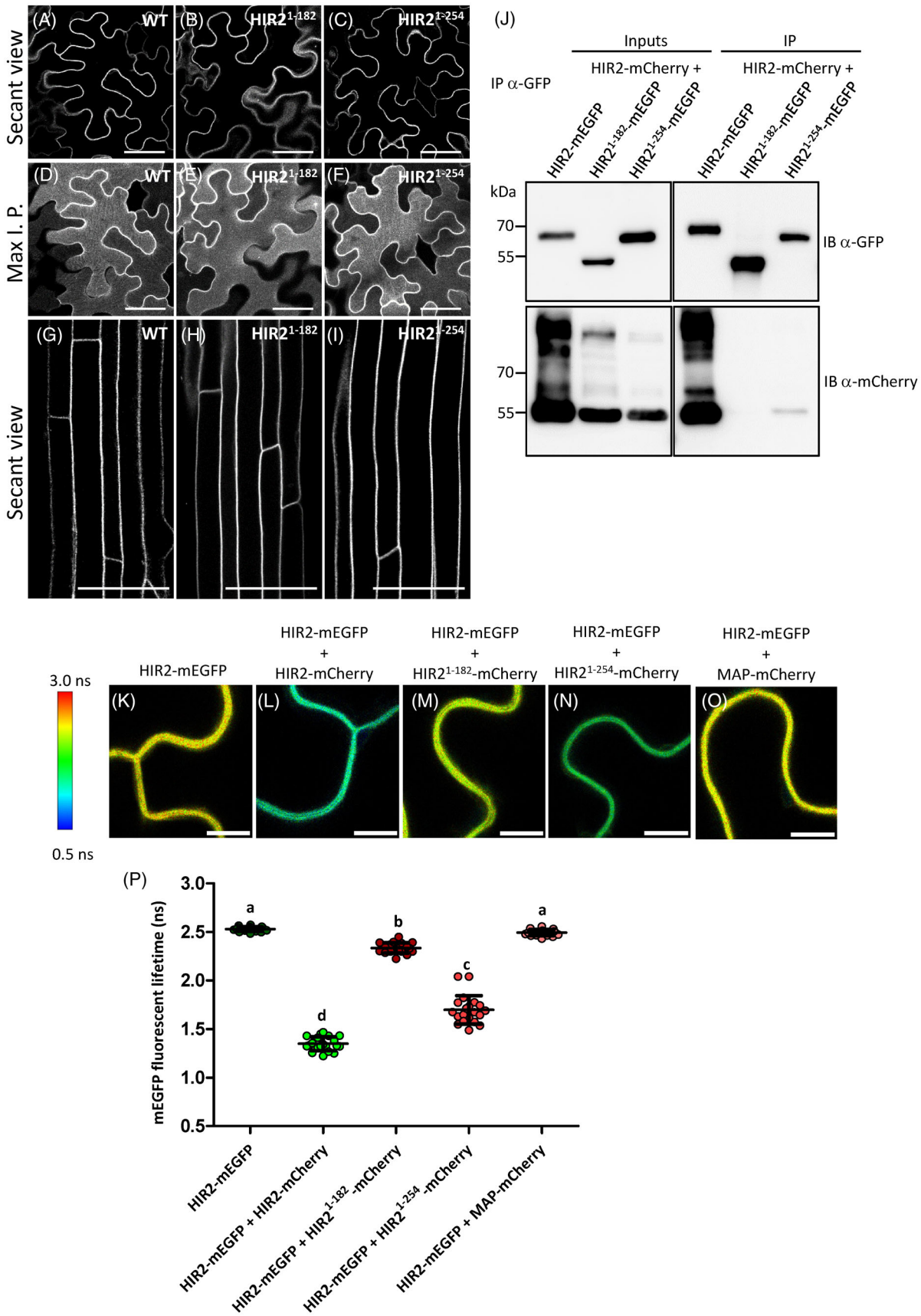

imaging microscopy (FRET-FLIM), a technic allowing to study protein–protein interactions in living plant cells (Bucherl et al., 2014). Compared with HIR2-mEGFP expressed alone, co-expression of HIR2-mCherry with HIR2-mEGFP in *N. benthamiana* leaf epidermal cells induced a strong reduction of HIR2-mEGFP fluorescence lifetime (T), from 2.53 to 1.35 ns (Figure 6K,L,P). This demonstrated a physical interaction between the two proteins in the PM, as expected. At the opposite, co-expression of $HIR2^{1\text{-}182}$-mCherry with HIR2-mEGFP induced a minor reduction of T ($T \approx 2.33$ ns), showing that the deletion of the whole HIR2 C-terminal part negatively influenced the interaction between the two proteins (Figure 6M,P). Deletion of the very C-terminal part of HIR2 ($HIR2^{1\text{-}254}$-mCherry) had a less pronounced effect, although it also affected interaction properties ($T \approx 1.70$ ns) (Figure 6N,P). Note that no significant decrease in T was observed when co-expressing HIR2-mEGFP with the PM localized MAP-mCherry protein with a value of ≈2.49 ns (negative control for interaction; Figure 6O,P). Thus, FRET-FLIM experiments confirmed the results of co-IP (Figure 6J), highlighting that the C-terminal part of HIR2 is required for HIR2–HIR2 protein interaction.

To go further in the study of the role of HIR2 C-terminal domain in HIR2 homooligomerization, we used computational analyses. First, the HIR2 oligomeric assembly was modeled using Alphafold3 (https://doi.org/10.1093/bioinformatics/btw514), which indicated that the HIR2 complex preferentially consists of 14 HIR2 subunits (Figure 7A). In agreement with other SPFH domain-containing proteins (Ma et al., 2022), HIR2 complex was predicted to form a ring-shaped structure (Figure 7B). Within this assembly, the SPFH domains are arranged side by side, and the C-terminal coiled-coil domains are interwound. Second, to evaluate the role of the C-terminal region of HIR2 in oligomerization, we estimated binding affinity for both the complete HIR2 oligomeric assembly and the truncated variant $HIR2^{1\text{-}182}$, using the PRODIGY web server. The energy of the full assembly was calculated to be -370 kcal mol^{-1}, whereas the assembly with the C-terminally truncated protein showed a substantially reduced binding affinity of -193 kcal mol^{-1} (Figure 7B). The observed decrease in the energy following C-terminal deletion indicates that this region is critical for inter-subunit stabilization and is energetically essential for oligomer formation. We also took advantage of computational analyses to predict the orientation of HIR2 complex relative to the PM using PPM Web Server (https://doi.org/10.1002/pro.4219). Interestingly, the S-acylated residues C6 and C7 were found to face the PM (Figure 7C), in accordance with a role of S-acylation in HIR2 membrane association.

We then compared the capacity of HIR2, $HIR2^{1\text{-}182}$, and $HIR2^{1\text{-}254}$ fused to mEGFP to relocalize $HIR2^{C6A,C7A}$-mCherry to the PM when co-expressed in *N. benthamiana* leaf epidermal cells (Figure S13A–I) and quantified this phenomenon by measuring the partitioning of the fluorescence intensity for the different proteins between the PM and the cytoplasm (Figure S13J,K). While HIR2, $HIR2^{1\text{-}182}$ and $HIR2^{1\text{-}254}$ fused to mEGFP showed strong association with the PM without any difference detected between full-length and truncated protein versions (Figure S13J), the capacity to induce the PM relocalization of $HIR2^{C6A,C7A}$-mCherry was decreased for both $HIR2^{1\text{-}182}$-mEGFP and $HIR2^{1\text{-}254}$-mEGFP compared with HIR2-mEGFP (Figure S13K). In accordance with the different binding capacities previously determined for $HIR2^{1\text{-}182}$ and $HIR2^{1\text{-}254}$ (Figure 6), $HIR2^{1\text{-}182}$ was unable to induce a relocalization of $HIR2^{C6A,C7A}$-mCherry to the PM (Figure S13D–F,K), whereas a partial PM targeting of this protein occurs upon co-expression with $HIR2^{1\text{-}254}$ (Figure S13G–I,K).

Oligomerization of HIR2 is required for its nano-organization in the PM

To investigate the importance of oligomerization in HIR2 nanodomain organization, we performed TIRF microscopy on the PM of *N. benthamiana* leaf epidermal cells and Arabidopsis root epidermal cells expressing HIR2, $HIR2^{1\text{-}182}$, and $HIR2^{1\text{-}254}$ proteins fused to fluorophores. Contrary to WT HIR2 that arranged in nanodomains (Figure 8A,D), $HIR2^{1\text{-}182}$ displayed a diffuse localization in the PM (Figure 8B,E), illustrated by a strong reduction of its CV value (Figure 8G). $HIR2^{1\text{-}254}$ partially arranged in nanoclusters (Figure 8C,F), as attested by a CV value between the ones of WT HIR2 and $HIR2^{1\text{-}182}$ (Figure 8G). Then, we wondered if this massive change in the localization of $HIR2^{1\text{-}182}$ protein could be associated with a change in its dynamics in the PM. Therefore, HIR2 and $HIR2^{1\text{-}182}$ fused to mEOS2 were expressed in *N. benthamiana* leaf epidermal cells, followed by sptPALM analysis. The localization and displacement of single molecules of WT HIR2 and $HIR2^{1\text{-}182}$ were reconstructed and used to assess their instantaneous diffusion (Figure 8H,J–L). The diffusion of $HIR2^{1\text{-}182}$-mEOS2 protein ($D = 0.042 \pm 0.004$ μm^2 sec^{-1}) was much higher than that of HIR2-mEOS2 ($D = 0.0016 \pm 0.0001$ μm^2 sec^{-1}) (Figure 8H,J,K). MSD values were higher for $HIR2^{1\text{-}182}$-mEOS2 compared with HIR2-mEOS2, showing that $HIR2^{1\text{-}182}$ protein is more mobile than HIR2 in the PM (Figure 8L). In addition, clustering analysis on PALM images using Voronoï tessellation showed that the occurrence of molecules with high local density was higher for HIR2-mEOS2 compared with $HIR2^{1\text{-}182}$-mEOS2 (Figure 8I,M). These combined approaches of TIRF and sptPALM strongly suggest that interfering with HIR2 oligomerization affects HIR2 nanoclustering and diffusion in the PM.

To investigate deeper the role of the C-terminal part of HIR2 in nanodomain organization, we generated additional truncated and chimeric HIR2 proteins: (1) $HIR2^{Nter}$ that corresponds to the 17 first amino acids of HIR2

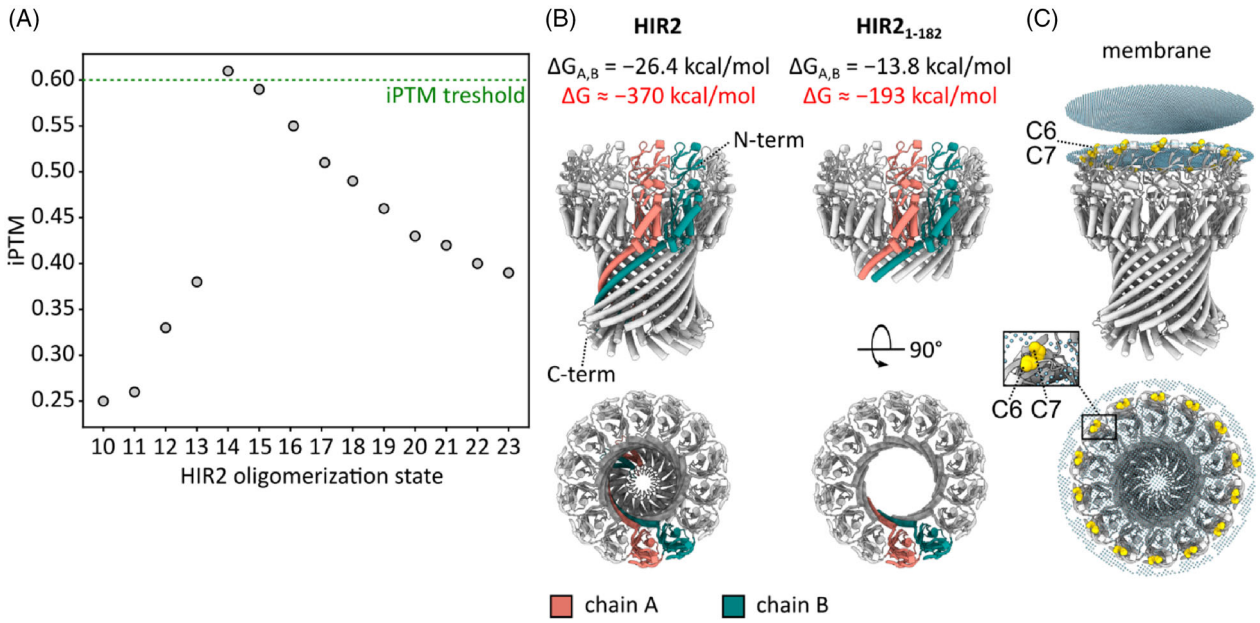

Figure 7. Prediction of HIR2 oligomeric state and impact of C-terminal deletion.
(A) Interface predicted template modeling (iPTM) scores for different oligomerization states of HIR2. The green dashed line indicates the 0.6 iPTM threshold, below which predictions are likely to fail or be incorrect. The 14-mer, which exhibited the highest overall iPTM score, was used for the binding affinity calculations shown in (B).
(B) Binding affinity ΔG calculated using the PRODIGY web server. The binding affinity between chains A and B ($\Delta G_{A,B}$) and thus the binding affinity for the whole complex (ΔG in red) is substantially lower for the full-length protein HIR2 than for HIR2$^{1-182}$, indicating a more thermodynamically favorable state.
(C) The HIR2 complex–membrane association predicted by the PPM Web Server corroborates the crucial role of the N-terminal parts and particularly the role of S-acylated residues C6 and C7.

including the S-acylation sites, (2) HIR2$^{Nter-Cter}$, a fusion between the 17 first amino acids and the C-terminal part of HIR2 (amino acids 183–285), (3) HIR2^{Cter} that corresponds to the C-terminal part of HIR2 (Figure 2U). When expressed in *N. benthamiana* leaf epidermal cells, HIR2^{Nter}-mEGFP solely displayed a PM localization as revealed by confocal microscopy, showing that a minimal sequence of HIR2 containing S-acylation sites is sufficient to ensure PM targeting (Figure 8P). HIR2$^{Nter-Cter}$-mCherry was targeted to the PM, although it was also detected in rare intracellular vesicles (Figure 8Q). By contrast, HIR2^{Cter}-mCherry displayed a cytosolic localization (Figure 8R). TIRF microscopy revealed that similarly to HIR2$^{1-182}$, HIR2^{Nter} fused to mEGFP displayed a diffuse localization in the PM (Figure 8T,U), with a CV value that was much lower than the one measured for WT HIR2 (Figure 8W). Interestingly, HIR2$^{Nter-Cter}$-mCherry protein was detected in PM clusters and the corresponding CV value was not different from the one of WT HIR2 (Figure 8V,W). This result showed that the addition of the C-terminal part of HIR2 to a PM targeted fluorescent protein is sufficient to induce its arrangement in nanodomains. Based on this set of data, we propose that HIR2 oligomerization through its C-terminal part is essential for HIR2 organization in PM nanodomains.

HIR2 nanodomain organization is required for HIR2-mediated ROS burst in response to flg22

In various organisms, a rapid burst of ROS is a conserved process during the immune response. Interestingly, the overexpression of pepper CaHIR1 protein in Arabidopsis can induce the accumulation of H_2O_2 in plant tissues (Jung & Hwang, 2007) and, recently, the ROS burst triggered by flg22 was shown to be attenuated in Arabidopsis *hir2* mutant (Liu, Zhao, et al., 2024). To investigate whether HIR2 nanodomain organization is necessary for HIR2 functioning, we compared the ability of WT HIR2 and HIR2$^{1-182}$, which is still present in the PM but does not organize in nanodomains, to be implicated in the ROS burst in response to flg22. To do so, we quantified the apoplastic ROS production in tobacco leaf discs expressing either HIR2-mCherry, HIR2$^{1-182}$-mCherry or mCherry (negative control) under the control of *HIR2* promoter, treated or not with flg22, using a luminol/peroxidase-based method. ROS accumulation was measured by following the emitted luminescence that was normalized, for each leaf disc, to mCherry fluorescence intensity, that is, to the expression of the proteins of interest. Upon flg22 treatment, leaf discs expressing HIR2-mCherry displayed a rapid and higher ROS accumulation compared with leaf discs expressing

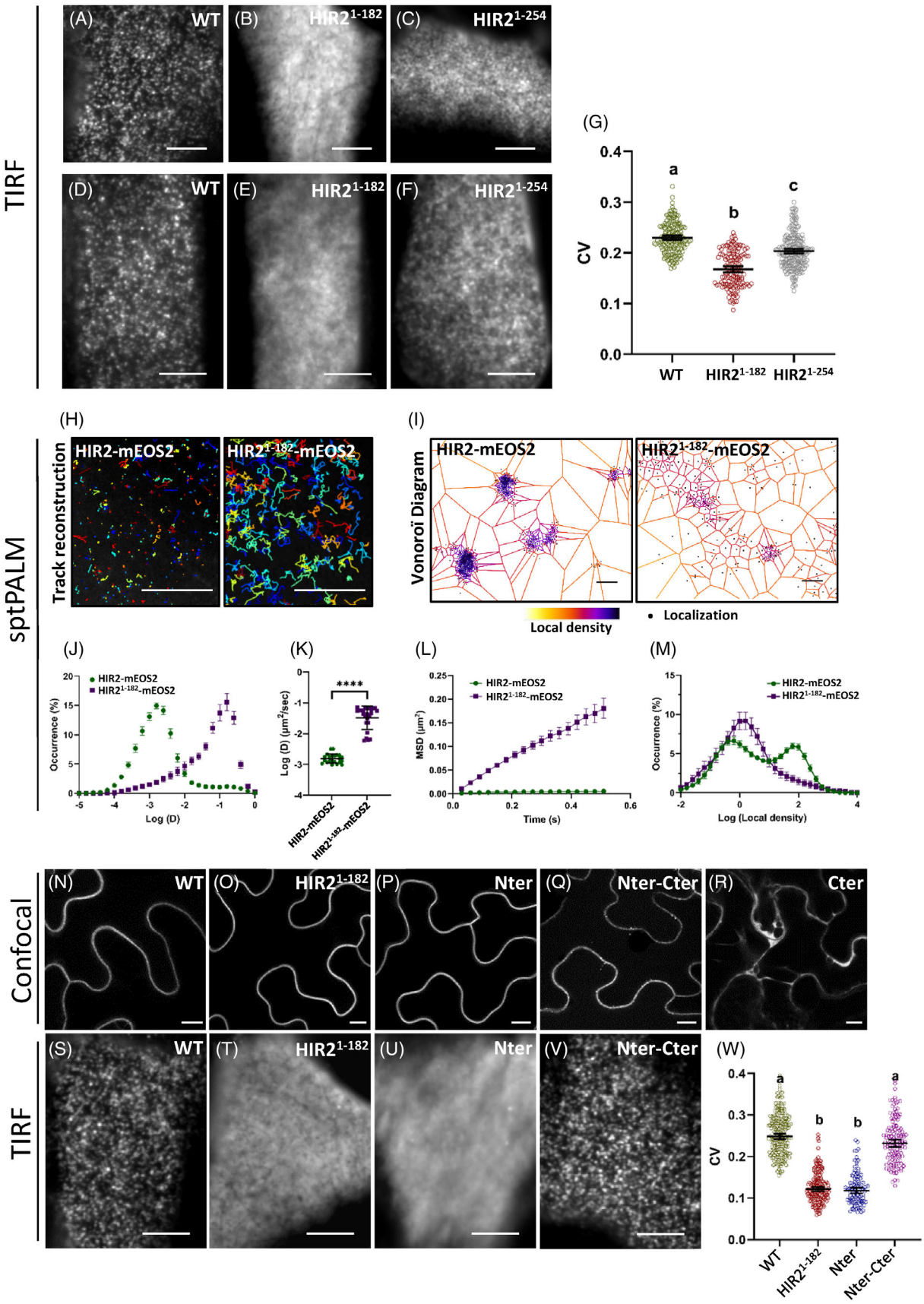

Figure 8. Oligomerization of HIR2 is required for its nano-organization in the plasma membrane (PM).
(A–M) Deletion of HIR2 C-terminus markedly reduced its PM clustering and diffusion restriction. The organization in the MP of HIR2-mEGFP (A, D), HIR2$^{1–182}$-mEGFP (B, E) and HIR2$^{1–254}$-mEGFP (C, F) proteins expressed under the control of *HIR2* promoter was analyzed by total internal reflection fluorescence (TIRF) microscopy. (A–C) *Nicotiana benthamiana* leaf epidermal cells. (D–F) Arabidopsis root epidermal cells. Arabidopsis seedlings were grown for 7 days on MS/2 medium. (G) Coefficients of variance (CV) of fluorescence intensity were calculated from TIRF experiments performed as in (D) to (F) on Arabidopsis root epidermal cells. Error bars correspond to a confidence interval of 95%. For each protein, between 150 and 240 intensity profiles from more than 30 cells from three independent biological replicates were analyzed. Letters indicate significant differences ($P < 0.05$, one-way ANOVA with *post-hoc* Tukey multiple comparison test). (H–M) Single-particle-tracking photoactivated localization microscopy (sptPALM) was performed on the PM of *N. benthamiana* leaf epidermal cells transiently expressing HIR2-mEOS2 and HIR2$^{1–182}$-mEOS2 to determine the trajectories of each single protein. (H) Image reconstruction of several tens of single HIR2-mEOS2 and HIR2$^{1–182}$-mEOS2 molecule trajectories indicated by different colors. (I) Voronoï tessellation of HIR2-mEOS2 and HIR2$^{1–182}$-mEOS2 molecule localization map from the same cells as in (H). The color code represents the local density of each molecule indicated by a black point. (J) Distribution of molecule instantaneous diffusion coefficient (D) (expressed in log [μm^2 sec^{-1}]) for HIR2-mEOS2 and HIR2$^{1–182}$-mEOS2. (K) Quantification of the diffusion of HIR2-mEOS2 and HIR2$^{1–182}$-mEOS2 molecules. (L) Mean square displacement (MSD) curves of HIR2-mEOS2 and HIR2$^{1–182}$-mEOS2 molecules over the time. (M) Distribution of molecule local density for HIR2-mEOS2 and HIR2$^{1–182}$-mEOS2. In (J–M), more than 20 cells from three independent biological replicates were analyzed. In (K), '****' represents $P < 0.0001$ in a *t*-test and error bars correspond to standard deviation.
(N–W) The C-terminal part of HIR2 is sufficient to induce nanodomain arrangements. The subcellular localization of HIR2-mCherry (N), HIR2$^{1–182}$-mCherry (O), HIR2^{Nter}-mEGFP (P), HIR2$^{Nter-Cter}$-mCherry (Q) and HIR2^{Cter}-mCherry (R) transiently expressed under the control of *HIR2* promoter in *N. benthamiana* leaf epidermal cells was analyzed by scanning confocal microscopy (secant views). HIR2^{Nter} and HIR2^{Cter} corresponds to the first 17 amino acids and the last 103 amino acids of HIR2, respectively, HIR2$^{Nter-Cter}$ is a fusion of the first 17 amino acids of HIR2 to the last 103 amino acids. (S–V) TIRF microscopy analysis on the PM of *N. benthamiana* leaf epidermal cells expressing the same proteins as in (N) to (Q). (W) Coefficients of variance (CV) of fluorescence intensity were calculated from TIRF experiments performed as in (S–V). For each protein, between 110 and 220 intensity profiles from more than 22 cells from three independent biological replicates were analyzed. Error bars correspond to a confidence interval of 95%. Letters indicate significant differences (*P*-value <0.05, one-way ANOVA with *post-hoc* Tukey multiple comparison test). Scale bars represent 5 μm (A–F; S–V), 10 μm (H, N–R), and 0.102 μm (I).

mCherry (Figure 9A,B). Interestingly, in response to flg22 stimulus, the production of ROS in leaf discs expressing HIR2$^{1-182}$-mCherry was much weaker than for HIR2-mCherry and not significantly different from the one observed in the negative control mCherry (Figure 9B). We concluded that HIR2 ectopic expression boosted apoplastic ROS accumulation in plant cells in response to flg22 and that this effect was canceled when HIR2 lost the ability to oligomerize and to organize in PM clusters (HIR2$^{1-182}$). Therefore, HIR2 nanodomain organization is a prerequisite for proper HIR2 functions in the cell.

DISCUSSION

Mono S-acylation of HIR2 is required for its PM localization

PM nanodomains emerged as signaling/regulation hubs involved in diverse biological processes (Hdedeh et al., 2025; Jolivet et al., 2025; Wang et al., 2024). However, so far, how these nanodomains are formed and maintained in plant cells remains largely unknown. Here, we sought to address this question by using the plant-specific SPFH protein HIR2 as a model.

We analyzed the role of two types of post-translational modifications, *N*-myristoylation and S-acylation, in HIR2 intracellular dynamics and nanodomain organization in Arabidopsis. Pharmacological treatment interfering with HIR2 S-acylation led to mis-localization of HIR2 in Arabidopsis root epidermal cells (Figure 3). In addition, HIR2^{C6A,C7A} mutated protein was no more S-acylated in Arabidopsis transgenic lines (Figure 3), which triggers its retention inside the cell (Figure 2). Similar results were previously obtained by transiently overexpressing HIR2^{C6S,C7S}-GFP in Arabidopsis protoplasts (Liu et al., 2021). However, it is important to mention that caution should be taken with protoplasts when studying PM nanodomain-organized proteins, because the cell wall plays an important role in the dynamics of such proteins, including HIR (Danek et al., 2020; Hosy et al., 2015; McKenna et al., 2019). Interestingly, we revealed that HIR2 is mono S-acylated on either C6 or C7 (Figure 3). This interchangeability in HIR2 S-acylation sites probably explains why HIR2^{C6A} and HIR2^{C7A} mutated proteins display normal PM localization and nanodomain organization (Figures 2 and 3). In addition, we showed that the very N-terminal part of HIR2 that carries the S-acylation sites is sufficient to drive a GFP protein to the PM (Figure 8), strengthening the role of S-acylation in HIR2 trafficking. Interestingly, the localization of the S-acylated residues C6 and C7 facing the PM in HIR2 complex, as determined by computational analysis, is in line with a role of S-acylation in HIR2 membrane association/targeting (Figures 7C and 10). Why HIR2 is mono S-acylated whereas both C6 and C7 can be S-acylation sites remains an open question. Interestingly, a site-specific analysis of neuronal protein S-acylation in mouse revealed that S-acylation sites on transmembrane proteins were enriched for di-cysteine motifs (CC), each cysteine could be S-acylated (Collins et al., 2017). We also analyzed a putative implication of C58 in HIR2 dynamics since this cysteine residue was proposed to be S-acylated (Kumar et al., 2022). However, in our experimental conditions, C58 likely did not undergo S-acylation (Figure 3) and had neither a role in HIR2 PM localization, nor in its nanodomain organization (Figures 2 and 4). HIR2^{C6A,C7A} mutated protein still associated with intracellular membranes (Figure S6), suggesting that lipidations are not the sole way to anchor HIR2 in membranes. Therefore, HIR2 may contain specific lipid interaction motifs as reported for

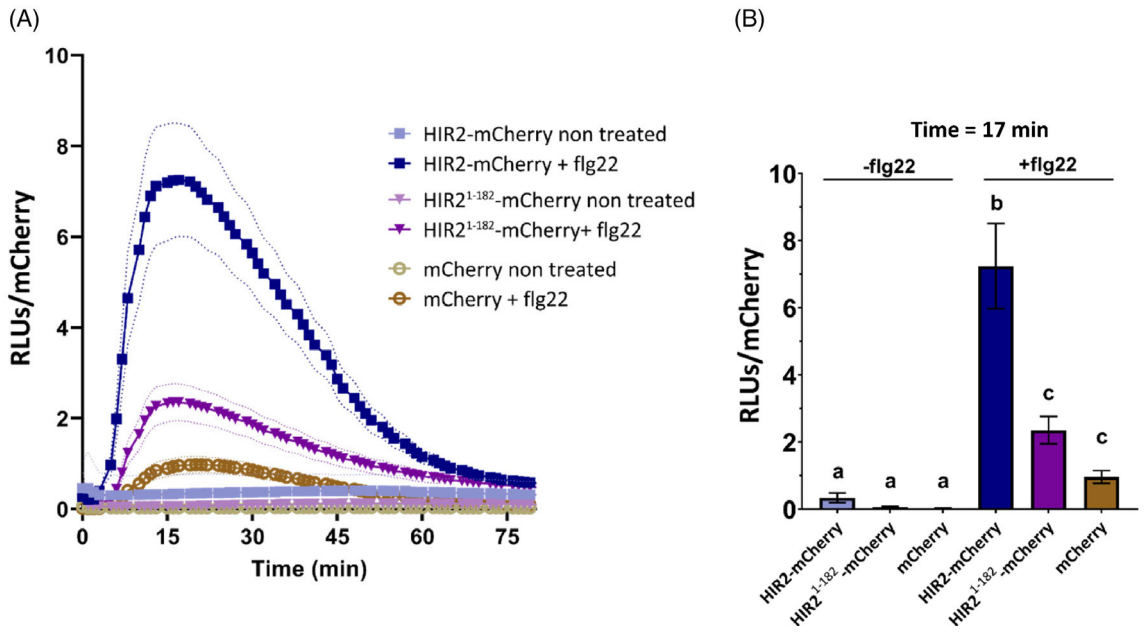

Figure 9. HIR2-stimulated oxidative burst in response to flg22 required HIR2 nanodomain organization.
(A, B) The production of apoplastic reactive oxygen species (ROS) was measured with a luminol-based assay in *Nicotiana benthamiana* leaf discs expressing the following proteins: HIR2-mCherry, HIR2$^{1-182}$-mCherry and mCherry (negative control). (A) Leaf discs were treated or not with 100 nM flg22 and ROS accumulation was measured by following the emitted luminescence every 1 min for 80 min. The emitted luminescence was normalized to the quantity of HIR2-mCherry, HIR2$^{1-182}$-mCherry and mCherry, estimated via mCherry fluorescence, and expressed in relative light units (RLUs). Curves show mean values with discontinued lines representing SE. A representative experiment among three independent biological experiments is shown. (B) The average ROS accumulation at 17 min (maximum of the peak) was measured for three independent biological experiments performed as in (A). Error bars represent SE. Letters indicate statistically significant differences between the different proteins that were expressed (ANOVA, multiple comparisons *post-hoc* Tukey's method at *P*-value <0.05). For each protein, 12 and 22 leaf discs for non-treated and flg22-treated conditions were analyzed, respectively.

animal SPFH proteins that can bind to sterols (Huber et al., 2006). WT HIR2 protein could induce the relocalization of HIR2^{C6A,C7A} to PM nanodomains via oligomerization (Figure S11), showing that in these experimental settings not all the HIR2 subunits needed to be S-acylated among a complex to be targeted to the PM. Whether HIR2 S-acylation is systematic in plant cells or concerns a part of HIR2 subunits remains at this stage an open question. In our PEG-shift assay, we observed that a part of WT HIR2 protein did not appear to be S-acylated (Figure 3), but, as previously mentioned, we cannot exclude that it may result from an incomplete binding of mPEG-Mal during the PEG-shift procedure. In addition, non-S-acylated HIR2 could correspond to newly synthesized protein, not yet S-acylated, or to de-S-acylated HIR2. S-acylation is performed by protein S-acyl transferases that are localized in diverse membrane compartments including ER, Golgi, PM, vesicles and tonoplast (Batistic, 2012). This indicates that proteins can be S-acylated during the maturation processes (ER, Golgi), during protein sorting and trafficking processes (Golgi and vesicles), or after arriving to targeting compartments, such as the PM (Li et al., 2022). Among others, S-acylation can be crucial for ER to PM trafficking (Batistic et al., 2008), but also for stable residence of proteins in the PM (Liu, Qu, et al., 2024). So far, in which subcellular compartment HIR2 is S-acylated remains unknown. In addition, although we clearly demonstrated that S-acylation is required for HIR2 PM localization, whether S-acylation is required for HIR2 trafficking to the PM or solely for its association with the PM remains to be determined. A first hypothesis is that HIR2 may be S-acylated in the PM to ensure its stable anchoring. A second hypothesis is that HIR2 may be S-acylated in an unidentified endomembrane compartment, which would allow its subsequent PM targeting. This hypothesis is supported by the observation that HIR2^{C6A,C7A}, that is trapped inside the cell in a membrane compartment, can be rescued to the PM by WT S-acylated HIR2 (Figure S11).

HIR2 was demonstrated to be *N*-myristoylated on G2 (Majeran et al., 2018), a result we confirmed here by mass spectrometry using HIR2-mCherry fusion protein (Figure S3). Some proteins bear both *N*-myristoylation and proximal S-acylation in their N-terminal part and this combination of lipidations is required for their PM targeting as exemplified by the plant calcineurin B–like protein 1 (CBL1) (Batistic et al., 2008). Interestingly, *N*-myristoylation can be a prerequisite for S-acylation, as shown for the plant GTPase Ara6 (Ueda et al., 2001). Surprisingly, we observed that HIR2^{G2A} mutated protein was properly targeted to the PM (Figure 2) and displayed a similar S-acylation profile

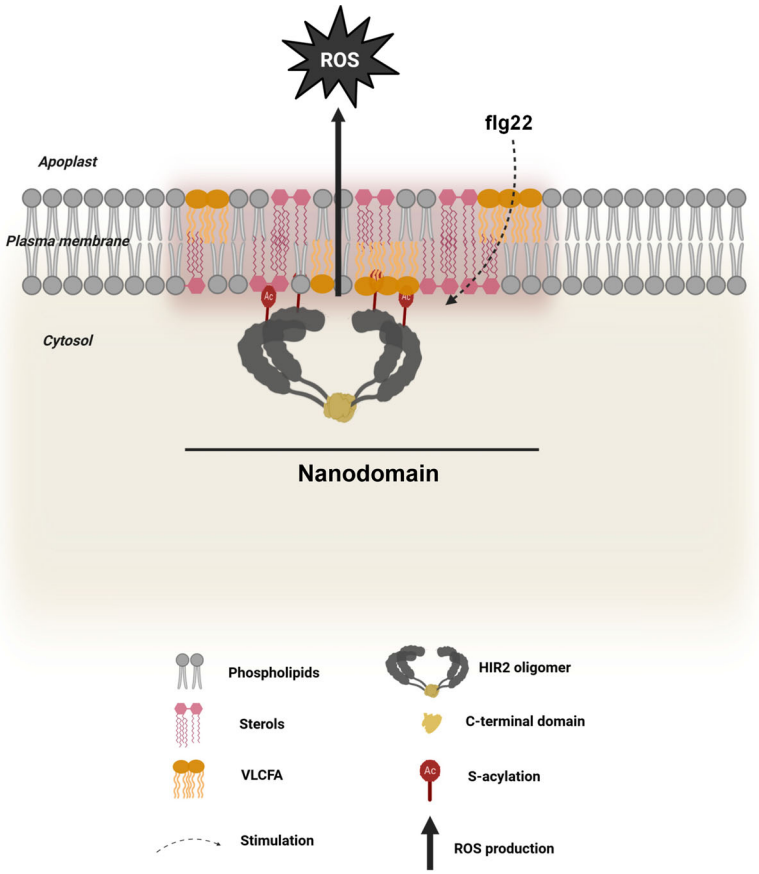

Figure 10. Tentative model.
HIR2 is mono S-acylated on N-terminally-located C6 or C7 which insures HIR2 membrane association/targeting. The oligomerization of HIR2 through its C-terminal domain determines the organization of HIR2 into plasma membrane (PM) nanodomains. In addition, sterols and very long chain fatty acids (VLCFA) are also required for HIR2 nanodomain organization in the PM. HIR2 can stimulate the apoplastic reactive oxygen species (ROS) burst induced by the bacterial peptide flg22 and this phenomenon is dependent on its arrangement in nanodomains. Note that the molecular mechanisms involving HIR2 in ROS production remain unknown. For clarity HIR2 is represented as a tetramer, although computational analyses suggest the presence of 14 monomers in HIR2 complex. This model was created using BioRender.

compared with WT HIR2 (Figure 3), ruling out the possibility that HIR2 *N*-myristoylation influences its S-acylation. Therefore, HIR2 dynamics is not canonically influenced by *N*-myristoylation. In addition, the normal clustering pattern of HIR2^{G2A} mutated protein in the PM excluded a possible role of this lipidation in HIR2 nanodomain organization (Figure 4). Interestingly, apart from membrane association, *N*-myristoylation is also involved in protein–protein interaction and protein activation (Wright et al., 2011; Zhu et al., 2019), giving some clues about a putative cellular function of HIR2 *N*-myristoylation.

We highlighted that HIR2 PM targeting likely relies on mechanisms independent of the COPII machinery (Figure S7), similarly to what was shown for the nanodomain-organized protein StREM1.3 (Gronnier et al., 2017). However, StREM1.3 is targeted to the PM from the cytosol, whereas our results suggest that HIR2 traffics through an intracellular membrane compartment since cell fractionation experiments highlighted that HIR2^{C6A,67A} associates with membranes (Figure S6). Despite our efforts, the identity of this compartment remains to be determined (Figures S7 and S8). We believe that the membranes where HIR2^{C6A,C7A} protein is trapped are probably on the natural pathway taken by HIR2 to reach the PM since WT HIR2 can encounter HIR2^{C6A,C7A} and relocalize it to the PM (Figure S11).

S-acylation was shown to promote the segregation of the transmembrane protein linker for activation of T cells (LAT) into membrane domains in giant PM vesicles isolated from animal cells (Levental et al., 2010). In addition, S-acylation drives the association of the membrane protein spike from SARS-CoV-2 with ordered lipid domains (Mesquita et al., 2021). In plants, the role of S-acylation in the targeting of proteins into nanodomains remains elusive (Jaillais & Ott, 2020). Interestingly, the S-acylation of remorins was shown to be required for their PM targeting

but not for their organization in nanodomains (Konrad et al., 2014). Here, we demonstrated that the N-terminal part of HIR2 carrying the S-acylation sites can drive a GFP to the PM but does not induce its clustering in nanodomains (Figure 8), showing that the S-acylation of HIR2 is not sufficient for its nanodomain organization. However, since HIR2^{C6A} and HIR2^{C7A} are normally S-acylated and because HIR2^{C6A,C7A} is retained intracellularly, it is difficult to conclude on a putative contribution of S-acylation to the HIR2 clustering process in the PM.

PM lipid composition influences HIR2 organization

We showed that proper sterol composition is required for the nanoclustering of HIR2 in the PM of Arabidopsis root epidermal cells (Figures 5 and 10). This is in accordance with a role of sterols in the PM dynamics of another HIR isoform, HIR1, that was previously reported using the sterol-depleting agent mβCD (Lv et al., 2017). Our results reinforce the notion that in plant cells, sterols play a key role in protein nano-organization as highlighted in the past (Cao et al., 2020; Grison et al., 2019; Gronnier et al., 2017). The reduction of HIR2 clustering following FEN treatment was not accompanied by a higher mobility of HIR2 molecules in the PM (Figure 5). Therefore, nanodomain organization and low lateral mobility of proteins are not necessarily correlated. VLCFA are essential lipids that play a structural role in the PM (Batsale et al., 2021). Altering the composition of VLCFA dramatically reduced the clustering of HIR2 in the PM of Arabidopsis root epidermal cells, which was accompanied by a strong increase in the mobility of HIR2 molecules (Figures 5 and 10), arguing for an important role of VLCFA in HIR2 nanodomain organization. VLCFA-containing lipids include sphingolipids and PS. So far, our pharmacological approach does not allow us to identify precisely which lipid(s) bearing a VLCFA is/are involved in HIR2 nano-organization. PS constitutes a very interesting candidate since this lipid can arrange in nanoclusters and was shown to stabilize ROP6 protein in PM nanodomains (Platre et al., 2019).

The oligomerization of HIR2 through its C-terminal part determines the organization of HIR2 into PM nanodomains, which is required for its proper function

Combining protein–protein interaction tests, we revealed that the C-terminal part of HIR2 is essential for HIR2 oligomerization (Figures 6 and 10). In addition, Alphafold3 modeling strongly suggests that HIR2 C-terminal domains are interwound and that their deletion substantially reduces the binding affinity of the HIR2 complex (Figure 7A,B). Our results in combination with other works reinforce the prominent function of the C-terminal part of SPFH proteins in their oligomerization (Solis et al., 2007; Umlauf et al., 2006; Yu et al., 2017). However, HIR proteins carry additional oligomerization domains since valine 157 present in the SPFH domain of Arabidopsis HIR4 isoform is important for HIR4 oligomerization (Liu, Zhao, et al., 2024). Although the exact oligomeric state of HIR2 complex remains to be experimentally determined, our Alphafold3 modeling strongly suggests that the HIR2 complex is preferentially composed of 14 copies arranged in a ring-shaped structure (Figure 7). These results are consistent with data on other SPFH proteins that form very large oligomers, 12 copies of HflK–HflC dimers in bacteria and 22 pairs of Flot1 and Flot2 subunits in humans (Fu & MacKinnon, 2024; Ma et al., 2022). We showed that the C-terminal part of HIR2 is dispensable for PM targeting and that indeed the 17 first amino acids of HIR2 were sufficient to drive a fluorescent protein to the PM (Figure 8). However, the C-terminal part of HIR2 is crucial for the organization of HIR2 in nanodomains since: (i) sequential deletions of the C-terminal part attenuated (HIR2$^{1-254}$) or totally abolished (HIR2$^{1-182}$) HIR2 nanoclustering, (ii) the C-terminal part of HIR2 artificially targeted to the PM arranged into clusters (HIR2$^{Nter-Cter}$; Figure 8). We propose that HIR2 oligomerization is necessary and sufficient for the organization of HIR2 into PM nanodomains (Figure 10). A crucial role for oligomerization in the arrangement into nanodomains could be probably extended to other plant proteins such as remorins (Bariola et al., 2004; Legrand et al., 2019; Martinez et al., 2019; Perraki et al., 2012). Abolishing HIR2 nanoclustering trough a deletion of the C-terminal part considerably increase the lateral mobility of HIR2 single molecules in the PM (Figure 8). This result is in accordance with data showing that mutated human Stomatin proteins, which cannot oligomerize any more, display an increased mobility in the PM, suggesting a conserved mechanism between plant and animals (Umlauf et al., 2006).

HIR2 protein is a positive actor of plant immunity, although the underlying molecular mechanisms remain largely unknown. Here, we showed that HIR2 overexpression stimulated apoplastic ROS accumulation in plant cells in response to flg22, a mechanism that required HIR2 oligomerization and nanodomain organization in the PM (Figures 9 and 10). This result is in line with recent work showing that the oligomerization of Arabidopsis HIR4 was essential for its role in mediating immunity via a regulation of ROS burst (Liu, Zhao, et al., 2024). SPFH proteins were proposed to act as scaffolding proteins in membrane nanodomains (Langhorst et al., 2005). Our data showing that HIR2 possesses the intrinsic property, through oligomerization, to arrange in nanoclusters support this concept of nanodomain structuration. HIR2 may interact with and recruit proteins in specific nanodomains, such as some proteins involved in plant immunity that were shown to physically interact with HIR (Jung & Hwang, 2007; Lv et al., 2017; Qi et al., 2011; Zhou et al., 2009). In the future, it will be interesting to determine how HIR-containing

nanodomains may act as hubs implicated in the defense against pathogens, notably by influencing ROS production. Interestingly, although HIR2 and remorins are both implicated in plant immunity (Qi et al., 2011; Raffaele et al., 2009), they are spatially segregated in the PM (Figure 1), suggesting that they act in different pathways.

A long-standing question in the field of membrane nanodomains is whether proteins are targeted to preexisting lipid-mediated nanodomains or if they actively organize their lipid environment through protein-lipid interactions, although these two hypotheses are not obligatorily exclusive (Gouguet et al., 2021). Interestingly, overexpression of remorins in plant cells modifies the local membrane order (Huang et al., 2019), suggesting that these proteins can influence their lipid environment. In addition, Legrand and coworkers showed that *S. tuberosum* StREM1.3 can organize lipid nanodomains, even in the absence of preexisting lipid domains (Legrand et al., 2023). By forming large multimeric complexes and binding to specific lipids, animal SPFH proteins were hypothesized to actively form nanodomains enriched in certain lipids (Browman et al., 2007). Since HIR2 actively participates in the formation of nanodomains and probably interacts with lipids as stated above, we anticipate that HIR2 may play a role in lipid clustering, although experimental evidence is needed. Interestingly, bacteria and human SPFH proteins were revealed to assemble in very large circular complexes that delimit a membrane domain of about 20–30 nm in diameter, which could de facto allow the segregation of lipids but also proteins (Fu & MacKinnon, 2024; Gao et al., 2025; Ma et al., 2022).

MATERIAL AND METHODS

Genetic constructions

All the constructs used in this work were obtained using the Multi-Site Gateway® Three-Fragment Vector Construction system (Life Technologies, Villebon-sur-Yvette, France), as detailed in Supporting Information S1—Supporting experimental procedures. The primer sequences are indicated in Table S1. p35S::Sar1(DN)-YFP, p35S::HDEL-pHluorine, pUBQ10::Rhal-mCherry, pUBQ10::ST-RFP, pVHAa1::VHAa1-RFP, p35S::GFP-SYP61 vectors were previously described (daSilva et al., 2004; Geldner et al., 2009; Hasegawa et al., 2022; Lupanga et al., 2020; Moreau et al., 2021).

Arabidopsis transgenic lines and growth conditions

Arabidopsis thaliana Col-0 ecotype was transformed with different genetic constructions by the floral dipping technique. Arabidopsis transgenic line expressing *35S::GFP-StREM1.3* was previously described (Legrand et al., 2023). Arabidopsis transgenic lines co-expressing *35S::GFP-StREM1.3*, *pREM1.2::YFP-REM1.2*, or *pREM1.3::YFP-REM1.3* (Jarsch et al., 2014) with *pHIR2::HIR2-mCherry* were obtained by crossing. Arabidopsis plants were vertically grown in sterile conditions at 21°C with 16 h light/8 h dark cycles with a light intensity of 90 μmol m^{-2} sec^{-1} using Philips 17W F17T8/TL741 bulbs. The plant growth medium used was half-strength Murashige and Skoog (MS/2) medium containing 1% sucrose and 1% agar.

Transient expression of proteins in *N. benthamiana* leaves

Leaves from 4-week-old plants of *N. benthamiana* were agroinfiltrated with *Agrobacterium tumefaciens* strain GV3101 suspensions of optical density 0.6–0.9, as previously described (Jay et al., 2023). After 2–3 days, infected leaves were collected for microscopy and/or biochemistry analysis.

Pharmacological treatments

Nine-day-old Arabidopsis seedlings grown on MS/2 solid medium were transplanted onto plates with the same solid medium supplemented with 2-BP (10 μM) for 7 h, FEN (50 μg ml^{-1}) for 24 h (Gronnier et al., 2017), or MTZ (100 nM) for 48 h (Grison et al., 2019). Since these drugs were diluted 4000 times from stock solutions in DMSO, 4000 times diluted DMSO was used as mock treatment.

Co-immunopurifications

co-IP were performed on 500 mg of *N. benthamiana* leaves transiently co-expressing HIR2-mCherry with HIR2-mEGFP, $HIR2^{1\text{-}182}$-mEGFP, or $HIR2^{1\text{-}254}$-mEGFP proteins, as previously described (Martin-Barranco et al., 2020). For details, see Supporting Information S1—Supporting experimental procedures.

Immunopurification of HIR2-mCherry for mass spectrometry analysis

Immunopurification of HIR2-mCherry was performed on 1 g of 10-day-old Arabidopsis plantlets expressing HIR2-mCherry under the control of *HIR2* promoter as previously described (Martin-Barranco et al., 2020). For details, see Supporting Information S1—Supporting experimental procedures.

Mass spectrometry: sample preparation, analysis, and identification

Immunopurified HIR2-mCherry was loaded on a 10% precast gel (Bio-Rad, Marnes-la-Coquette, France) and submitted to a 15 min migration at 100 V for a 1 cm migration. Then, sample preparation, mass spectrometry analysis and peptide identification were performed as previously described (Berger et al., 2022). For details, see Supporting Information S1—Supporting experimental procedures.

Cell fractionation

Cell fractionation was performed on 200 mg of *N. benthamiana* leaves transiently expressing WT HIR2 and HIR2-mutated proteins fused to mCherry, as previously described (Zelazny et al., 2013). For details, see Supporting Information S1—Supporting experimental procedures.

PEG-shift assay

The S-acylation of HIR2 and HIR2-mutated proteins was analyzed through a PEG-shift assay adapted from the protocol developed by Percher et al. (2017), as detailed in Supporting Information S1—Supporting experimental procedures.

Immunodetections

Immunoblot analyses were performed as previously described (Barberon et al., 2011). Antibodies and dilutions are described in Supporting Information S1—Supporting experimental procedures.

Measurement of apoplastic ROS in *N. benthamiana* leaf discs

Measurements of apoplastic ROS production following flg22 treatment in *N. benthamiana* leaf disks transiently expressing HIR2-mCherry, HIR2$^{1-182}$-mCherry, and mCherry under the control of the *HIR2* promoter were performed as follows,No significant differences were found mainly as described by D'Ambrosio et al. (2017). Two days post-infiltration, expression of mCherry fusion proteins and mCherry alone was verified by confocal microscopy as described below. Then, leaf discs of 4 mm in diameter were generated with a cookie cutter and incubated for 24 h in 96-well plates containing sterile S Buffer (10 mM MES-KOH pH 6.1 mM $CaCl_2$, 1 mM KCl and 1% sucrose). Afterwards, the discs were washed three times with R buffer (10 mM HEPES-KOH pH 8) and then incubated with T buffer (10 mM HEPES-KOH pH 8, 20 mM Luminol L-012 [Sigma, Saint-Quentin-Fallavier, France], and 10 mM horseradish peroxidase [Sigma]). Subsequently, apoplastic ROS production of leaf discs treated or not with 100 nM flg22 was evaluated by measuring the luminescence generated by the oxidation of the luminol in the presence of ROS for 80 min, using a CLARIOstar plate reader machine (BMG-Lab tech, Champigny-sur-Marne, France). For normalization, mCherry fluorescence of all discs was measured at 614 nm with the CLARIOstar after excitation at 580 nm.

Confocal and spinning-disk microscopy

Seedlings were mounted in a drop of liquid medium of the same composition as the medium used for a given treatment. A laser scanning microscope (SP8, Leica, Wetzlar, Germany) equipped with a HyD detector or a spinning-disk microscope (Dragonfly, Andor, Abingdon-on-Thames, UK) equipped with EMCCD iXon888 camera (Andor) were used for imaging. 40× Plan Apo (N. A. 1.1, water immersion), and 100× Plan Apo (N.A. 1.45, oil immersion) objectives were used with the laser scanning microscope, and the spinning-disk microscope, respectively. 488 and 561 nm laser lines were used for mEGFP or YFP, and mCherry excitation, respectively.

Image analysis

Following spinning-disk acquisitions, nanodomain co-localization was evaluated with JACoP2 plugin (Bolte & Cordelieres, 2006) in Fiji (Schindelin et al., 2012) on square regions of interest (ROIs) of five times 5 μm. Rotation of one channel by 90° with respect to the other was performed as a control for random co-localization. CV of signal intensities (Retzer et al., 2017) in a linear probe of 10 μm was determined in order to assess the level of clustering as in Danek et al. (2020). Maximum intensity projections, average intensity projections, and orthogonal projections were constructed in Fiji.

For confocal co-localization analyses between HIR2^{C6A,C7A} and markers of intracellular compartments, *z*-stacks of 5–6 optical sections were acquired and maximum intensity projections were generated using ImageJ. PCC was calculated on selected ROIs using JACoP2.

Subcellular localization partitioning between the PM and the cytoplasm (PM/cyto) was calculated as previously described (Simon et al., 2016). PM/cyto-values were determined for HIR2^{C6A,C7A}-mCherry upon co-expression with HIR2-mEGFP, HIR2$^{1-182}$-mEGFP, and HIR2$^{1-254}$-mEGFP and divided by the corresponding signal intensities of HIR2-mEGFP, HIR2$^{1-182}$-mEGFP, and HIR2$^{1-254}$-mEGFP at the PM (PM/cyto/GFP). This allowed to take the protein level of WT/truncated HIR2 tagged with mEGFP co-expressed with HIR2^{C6A,C7A}-mCherry for each cell analyzed.

TIRF microscopy

TIRF microscopy was performed using the same inverted Zeiss microscope as for sptPALM as previously described (Smokvarska et al., 2023). For details, see Supporting Information S1—Supporting experimental procedures.

Single-particle tracking photoactivated localization microscopy

The sptPALM experiments were conducted following the protocol outlined by Bayle et al. (2021), as detailed in Supporting Information S1—Supporting experimental procedures.

Single-particle tracking and Voronoï tessellation

Single molecules were individually localized and tracked using the ImageJ pluggin Trackmate 7 software (Ershov et al., 2022). Subsequently, the dynamic characteristics of these single emitters within cells were deduced from their tracks using custom-made analysis software developed in MATLAB (The MathWorks, Natick, MA, USA) (Bayle et al., 2021). The diffusion coefficient (*D*) for each track was computed by fitting the MSD curve accordingly (Bayle et al., 2021). For clustering analysis, the positions provided by Trackmate 7 for each mEOS2 detection served as inputs for the SR-Tesseler software, which in turn was used to generate a Voronoï diagram (Levet et al., 2015). Corrections for multiple detections of the same emitter were implemented based on recommendations from the same reference. The local densities of each track were computed as the inverse of their minimal surface.

Förster resonance energy transfer-fluorescence lifetime imaging microscopy

FRET-FLIM measurements were performed using a Leica Stellaris 8 Falcon confocal microscope equipped with a white light laser (WLL/SUPERCONTINUUM) on *N. benthamiana* leaf epidermal cells expressing HIR2-mEGFP (donor) alone or in combination with different mCherry fusion proteins (acceptors). Images were acquired using an HC PL APO CS2 40× water immersion objective. Image resolution was set to 1024 × 1024 pixels. mEGFP was excited at 488 nm and fluorescence emission was collected between 498 and 540 nm. mCherry was excited at 585 nm and emission was collected between 595 and 630 nm. Donor fluorescence lifetime (τ) analysis was performed using all detected photons, and τ values were extracted from pixel clusters using a phasor plot approach. Three independent biological replicates were performed.

Computational analysis of HIR2 oligomerization

HIR2 oligomerization states were predicted using the AlphaFold3 web server (Abramson et al., 2024), or Foldify, a local installation of AlphaFold3. Models were evaluated based on their iPTM (Interface predicted template modeling) scores, which estimate interaction confidence, and the highest scoring ones were selected for further analysis. For the resulting highest scoring model (the 14-mer), binding affinity, reflecting how strongly two protein chains interact, was then predicted using the PRODIGY web server (Vangone & Bonvin, 2015; Xue et al., 2016) for both full-length HIR2 and HIR2$^{1-182}$. The HIR2 complex–membrane association was predicted with the PPM Web Server (Lomize et al., 2022).

Statistical analysis

For microscopy experiments, a representative image is shown. Statistical analyses were performed using the software GraphPad Prism 7. The sample size and statistical tests used are mentioned in the figure legends.

ACKNOWLEDGMENTS

We thank Yvon Jaillais and Lionel Verdoucq for interesting scientific discussions. We also thank Marc Boutry and Nadine Paris for the anti-PMA2 antibody and p35S::HDEL-pHluorine vector, respectively. This work benefited from access to the optic facilities of the Integrated Biophysics and Structural Biology Platform (PIBBS). PIBBS is a GIS-IBISA platform and belongs to the French Infrastructure for France Bio-Imaging (FBI), supported by the National Research Agency (ANR-10-INBS-04-01). Mass spectrometry experiments were carried out using the facilities of the Montpellier Proteomics Platform (PPM, BioCampus Montpellier). We thank the Montpellier Ressources Imagerie (MRI) and the Histocytology and Plant Cell Imaging Platform (PHIV) for providing the microscope facility. Computational resources used for local AlphaFold3 calculations were provided by the e-INFRA CZ project (ID: 90254), supported by the Ministry of Education, Youth and Sports of the Czech Republic.

This work was funded by the French National Research Agency (ANR-18-CE20-0008, NUTRIR project and ANR-23-CE20-0022, HIRAQIM project to EZ) and has benefited from a French State grant (reference ANR-10-LABX-0040-SPS, to EZ) managed by the French National Research Agency under an Investments for the Future program (reference n° ANR-11-IDEX-0003-02). AM was funded by the French National Agency ANR CellOsmo (ANR-19-CE20-0008-01) and the I-Site 'Montpellier Université d'Excellence' OptoSens. SM was funded by the French National Research Agency (ANR-19-CE13-0021, PhosphoREM). Open access publication funding provided by COUPERIN CY26.

AUTHOR CONTRIBUTIONS

MD, OH, JA, JB, MN, HS, AM-B, CM, RP, AM, and EZ designed the research; MD, OH, JA, MN, JB, HS, AA, AM-B, CM, BD, RP, and EZ performed the experiments; MD, OH, JA, JB, MN, HS, AA, AM-B, J-BF, CM, GK, MN, RP, YB, VS, SM, AM, and EZ analyzed the data; MD, OH, JA, MN, J-BF, MN, RP, YB, VS, SM, AM, and EZ wrote the manuscript.

CONFLICT OF INTEREST

None of the authors have a conflict of interest to disclose.

DATA AVAILABILITY STATEMENT

The data that support the findings of this study are available from the corresponding author upon reasonable request.

SUPPORTING INFORMATION

Additional Supporting Information may be found in the online version of this article.

Figure S1. Expression territories and subcellular localization of HIR2 in *Arabidopsis thaliana*.

Figure S2. The anti-mCherry antibody specifically recognizes HIR2-mCherry fusion protein in plant protein extracts.

Figure S3. Identification of HIR2 N-terminal *N*-myristoylation.

Figure S4. Simultaneous mutations of C6 and C7 induce HIR2 intracellular retention.

Figure S5. HIR2 is mono S-acylated and simultaneous mutations of C6 and C7 abolish HIR2 S-acylation.

Figure S6. Point-mutated variants of HIR2 affected for S-acylation and *N*-myristoylation still associate with membranes.

Figure S7. HIR2 plasma membrane targeting relies on mechanisms independent of the secretory pathway.

Figure S8. $HIR2^{C6A,C7A}$ does not co-localize with different markers of intracellular compartments.

Figure S9. Fenpropimorph treatment alters the nanodomain organization of both HIR2-mCherry and GFP-StREM1.3 proteins at the plasma membrane in Arabidopsis root epidermal cells.

Figure S10. StREM1.3 nanodomain organization is not disturbed by metazachlor.

Figure S11. $HIR2^{C6A,C7A}$-mCherry is relocalized to plasma membrane nanodomains upon co-expression with the non-mutated HIR2 protein fused to EGFP.

Figure S12. The C-terminal part of HIR2 is required for oligomerization as revealed by co-immunopurifications.

Figure S13. Plasma membrane relocalization of $HIR2^{C6A,C7A}$-mCherry is ineffective upon co-expression with C-terminal deleted versions of HIR2.

Table S1. Primers used in this work.

Supporting Information S1. Supporting experimental procedures.

Video S1. spt-PALM analysis of the dynamics of HIR2-mEOS2 single molecules in the plasma membrane of Arabidopsis root epidermal cells.

REFERENCES

Abramson, J., **Adler, J.**, **Dunger, J.**, **Evans, R.**, **Green, T.**, **Pritzel, A.** ***et al.*** (2024) Accurate structure prediction of biomolecular interactions with AlphaFold 3. *Nature*, **630**, 493–500.

Barberon, M., **Zelazny, E.**, **Robert, S.**, **Conejero, G.**, **Curie, C.**, **Friml, J.** ***et al.*** (2011) Monoubiquitin-dependent endocytosis of the iron-regulated transporter 1 (IRT1) transporter controls iron uptake in plants. *Proceedings of the National Academy of Sciences of the United States of America*, **108**, E450–E458.

Bariola, P.A., **Retelska, D.**, **Stasiak, A.**, **Kammerer, R.A.**, **Fleming, A.**, **Hijri, M.** ***et al.*** (2004) Remorins form a novel family of coiled coil-forming oligomeric and filamentous proteins associated with apical, vascular and embryonic tissues in plants. *Plant Molecular Biology*, **55**, 579–594.

Batistic, O. (2012) Genomics and localization of the Arabidopsis DHHC-cysteine-rich domain S-acyltransferase protein family. *Plant Physiology*, **160**, 1597–1612.

Batistic, O., **Sorek, N.**, **Schultke, S.**, **Yalovsky, S.** & **Kudla, J.** (2008) Dual fatty acyl modification determines the localization and plasma membrane targeting of CBL/CIPK Ca^{2+} signaling complexes in Arabidopsis. *Plant Cell*, **20**, 1346–1362.

Batsale, M., **Bahammou, D.**, **Fouillen, L.**, **Mongrand, S.**, **Joubes, J.** & **Domergue, F.** (2021) Biosynthesis and functions of very-long-chain fatty acids in the responses of plants to abiotic and biotic stresses. *Cells*, **10**, 1284.

Bayle, V., **Fiche, J.B.**, **Burny, C.**, **Platre, M.P.**, **Nollmann, M.**, **Martiniere, A.** ***et al.*** (2021) Single-particle tracking photoactivated localization microscopy of membrane proteins in living plant tissues. *Nature Protocols*, **16**, 1600–1628.

Berger, N., **Demolombe, V.**, **Hem, S.**, **Rofidal, V.**, **Steinmann, L.**, **Krouk, G.** ***et al.*** (2022) Root membrane ubiquitinome under short-term osmotic stress. *International Journal of Molecular Sciences*, **23**, 1956.

Bolte, S. & **Cordelieres, F.P.** (2006) A guided tour into subcellular colocalization analysis in light microscopy. *Journal of Microscopy*, **224**, 213–232.

Browman, D.T., **Hoegg, M.B.** & **Robbins, S.M.** (2007) The SPFH domain-containing proteins: more than lipid raft markers. *Trends in Cell Biology*, **17**, 394–402.

Bucherl, C.A., **Bader, A.**, **Westphal, A.H.**, **Laptenok, S.P.** & **Borst, J.W.** (2014) FRET-FLIM applications in plant systems. *Protoplasma*, **251**, 383–394.

Bucherl, C.A., **Jarsch, I.K.**, **Schudoma, C.**, **Segonzac, C.**, **Mbengue, M.**, **Robatzek, S.** ***et al.*** (2017) Plant immune and growth receptors share common signalling components but localise to distinct plasma membrane nanodomains. *eLife*, **6**, e25114.

Cao, Y., **He, Q.**, **Qi, Z.**, **Zhang, Y.**, **Lu, L.**, **Xue, J.** ***et al.*** (2020) Dynamics and endocytosis of Flot1 in Arabidopsis require CPI1 function. *International Journal of Molecular Sciences*, **21**, 1552.

Chung, K.P., **Zeng, Y.** & **Jiang, L.** (2016) COPII paralogs in plants: functional redundancy or diversity? *Trends in Plant Science*, **21**, 758–769.

Collins, M.O., **Woodley, K.T.** & **Choudhary, J.S.** (2017) Global, site-specific analysis of neuronal protein S-acylation. *Scientific Reports*, **7**, 4683.

D'Ambrosio, J.M., **Couto, D.**, **Fabro, G.**, **Scuffi, D.**, **Lamattina, L.**, **Munnik, T.** ***et al.*** (2017) Phospholipase C2 affects MAMP-triggered immunity by modulating ROS production. *Plant Physiology*, **175**, 970–981.

Danek, M., **Angelini, J.**, **Malinska, K.**, **Andrejch, J.**, **Amlerova, Z.**, **Kocourkova, D.** ***et al.*** (2020) Cell wall contributes to the stability of plasma membrane nanodomain organization of *Arabidopsis thaliana* FLOTILLIN2 and HYPERSENSITIVE INDUCED REACTION1 proteins. *The Plant Journal*, **101**, 619–636.

Danek, M., **Valentova, O.** & **Martinec, J.** (2016) Flotillins, Erlins, and HIRs: from animal base camp to plant new horizons. *Critical Reviews in Plant Sciences*, **35**, 191–214.

daSilva, L.L., **Snapp, E.L.**, **Denecke, J.**, **Lippincott-Schwartz, J.**, **Hawes, C.** & **Brandizzi, F.** (2004) Endoplasmic reticulum export sites and Golgi bodies behave as single mobile secretory units in plant cells. *Plant Cell*, **16**, 1753–1771.

Demir, F., **Horntrich, C.**, **Blachutzik, J.O.**, **Scherzer, S.**, **Reinders, Y.**, **Kierszniowska, S.** ***et al.*** (2013) Arabidopsis nanodomain-delimited ABA signaling pathway regulates the anion channel SLAH3. *Proceedings of the National Academy of Sciences of the United States of America*, **110**, 8296–8301.

Ershov, D., **Phan, M.S.**, **Pylvanainen, J.W.**, **Rigaud, S.U.**, **Le Blanc, L.**, **Charles-Orszag, A.** ***et al.*** (2022) TrackMate 7: integrating state-of-the-art segmentation algorithms into tracking pipelines. *Nature Methods*, **19**, 829–832.

Fu, Z. & **MacKinnon, R.** (2024) Structure of the flotillin complex in a native membrane environment. *Proceedings of the National Academy of Sciences of the United States of America*, **121**, e2409334121.

Gao, J., **Sherpa, D.**, **Kupko, N.**, **Chino, H.**, **Zeng, J.** & **Shao, S.** (2025) Structures of human organellar SPFH protein complexes. *Nature Communications*, **16**, 10064.

Geldner, N., **Denervaud-Tendon, V.**, **Hyman, D.L.**, **Mayer, U.**, **Stierhof, Y.D.** & **Chory, J.** (2009) Rapid, combinatorial analysis of membrane compartments in intact plants with a multicolor marker set. *The Plant Journal*, **59**, 169–178.

Glebov, O.O., **Bright, N.A.** & **Nichols, B.J.** (2006) Flotillin-1 defines a clathrin-independent endocytic pathway in mammalian cells. *Nature Cell Biology*, **8**, 46–54.

Gouguet, P., **Gronnier, J.**, **Legrand, A.**, **Perraki, A.**, **Jolivet, M.D.**, **Deroubaix, A.F.** ***et al.*** (2021) Connecting the dots: from nanodomains to physiological functions of remorins. *Plant Physiology*, **185**, 632–649.

Grison, M.S., **Kirk, P.**, **Brault, M.L.**, **Wu, X.N.**, **Schulze, W.X.**, **Benitez-Alfonso, Y.** ***et al.*** (2019) Plasma membrane-associated receptor-like kinases relocalize to plasmodesmata in response to osmotic stress. *Plant Physiology*, **181**, 142–160.

Gronnier, J., **Crowet, J.M.**, **Habenstein, B.**, **Nasir, M.N.**, **Bayle, V.**, **Hosy, E.** ***et al.*** (2017) Structural basis for plant plasma membrane protein dynamics and organization into functional nanodomains. *eLife*, **6**, e26404.

Gronnier, J., **Gerbeau-Pissot, P.**, **Germain, V.**, **Mongrand, S.** & **Simon-Plas, F.** (2018) Divide and rule: plant plasma membrane organization. *Trends in Plant Science*, **23**, 899–917.

Grosjean, K., **Mongrand, S.**, **Beney, L.**, **Simon-Plas, F.** & **Gerbeau-Pissot, P.** (2015) Differential effect of plant lipids on membrane organization: specificities of phytosphingolipids and phytosterols. *The Journal of Biological Chemistry*, **290**, 5810–5825.

Hasegawa, Y., **Huarancca Reyes, T.**, **Uemura, T.**, **Baral, A.**, **Fujimaki, A.**, **Luo, Y.** ***et al.*** (2022) The TGN/EE SNARE protein SYP61 and the ubiquitin ligase ATL31 cooperatively regulate plant responses to carbon/nitrogen conditions in Arabidopsis. *Plant Cell*, **34**, 1354–1374.

Hdedeh, O., **Mercier, C.**, **Poitout, A.**, **Martiniere, A.** & **Zelazny, E.** (2025) Membrane nanodomains to shape plant cellular functions and signaling. *The New Phytologist*, **245**, 1369–1385.

Hemsley, P.A. (2015) The importance of lipid modified proteins in plants. *The New Phytologist*, **205**, 476–489.

Hemsley, P.A., **Weimar, T.**, **Lilley, K.S.**, **Dupree, P.** & **Grierson, C.S.** (2013) A proteomic approach identifies many novel palmitoylated proteins in Arabidopsis. *The New Phytologist*, **197**, 805–814.

Hinderhofer, M., **Walker, C.A.**, **Friemel, A.**, **Stuermer, C.A.**, **Moller, H.M.** & **Reuter, A.** (2009) Evolution of prokaryotic SPFH proteins. *BMC Evolutionary Biology*, **9**, 10.

Hosy, E., **Martiniere, A.**, **Choquet, D.**, **Maurel, C.** & **Luu, D.T.** (2015) Super-resolved and dynamic imaging of membrane proteins in plant cells reveal contrasting kinetic profiles and multiple confinement mechanisms. *Molecular Plant*, **8**, 339–342.

Huang, D., **Sun, Y.**, **Ma, Z.**, **Ke, M.**, **Cui, Y.**, **Chen, Z.** ***et al.*** (2019) Salicylic acid-mediated plasmodesmal closure via remorin-dependent lipid organization. *Proceedings of the National Academy of Sciences of the United States of America*, **116**, 21274–21284.

Huber, T.B., **Schermer, B.**, **Muller, R.U.**, **Hohne, M.**, **Bartram, M.**, **Calixto, A.** ***et al.*** (2006) Podocin and MEC-2 bind cholesterol to regulate the activity of associated ion channels. *Proceedings of the National Academy of Sciences of the United States of America*, **103**, 17079–17086.

Hurst, C.H., **Turnbull, D.**, **Xhelilaj, K.**, **Myles, S.**, **Pflughaupt, R.L.**, **Kopischke, M.** ***et al.*** (2023) S-acylation stabilizes ligand-induced receptor kinase complex formation during plant pattern-triggered immune signaling. *Current Biology*, **33**, 1588–1596.e1586.

Jaillais, Y., **Bayer, E.**, **Bergmann, D.C.**, **Botella, M.A.**, **Boutte, Y.**, **Bozkurt, T.O.** ***et al.*** (2024) Guidelines for naming and studying plasma membrane domains in plants. *Nature Plants*, **10**, 1172–1183.

Jaillais, Y. & **Ott, T.** (2020) The nanoscale organization of the plasma membrane and its importance in signaling: a proteolipid perspective. *Plant Physiology*, **182**, 1682–1696.

Jarsch, I.K., **Konrad, S.S.**, **Stratil, T.F.**, **Urbanus, S.L.**, **Szymanski, W.**, **Braun, P.** ***et al.*** (2014) Plasma membranes are subcompartmentalized into a plethora of coexisting and diverse microdomains in Arabidopsis and *Nicotiana benthamiana*. *The Plant Cell*, **26**, 1698–1711.

Jay, F., **Brioudes, F.** & **Voinnet, O.** (2023) A contemporary reassessment of the enhanced transient expression system based on the tombusviral silencing suppressor protein P19. *The Plant Journal*, **113**, 186–204.

Jolivet, M.D., **Deroubaix, A.F.**, **Boudsocq, M.**, **Abel, N.B.**, **Rocher, M.**, **Robbe, T.** ***et al.*** (2025) Interdependence of plasma membrane nanoscale dynamics of a kinase and its cognate substrate underlies Arabidopsis response to viral infection. *eLife*, **12**, RP90309.

Jung, H.W. & **Hwang, B.K.** (2007) The leucine-rich repeat (LRR) protein, CaLRR1, interacts with the hypersensitive induced reaction (HIR) protein, CaHIR1, and suppresses cell death induced by the CaHIR1 protein. *Molecular Plant Pathology*, **8**, 503–514.

Konrad, S.S., **Popp, C.**, **Stratil, T.F.**, **Jarsch, I.K.**, **Thallmair, V.**, **Folgmann, J.** ***et al.*** (2014) S-acylation anchors remorin proteins to the plasma membrane but does not primarily determine their localization in membrane microdomains. *New Phytologist*, **203**, 758–769.

Kumar, M., **Carr, P.** & **Turner, S.R.** (2022) An atlas of Arabidopsis protein S-acylation reveals its widespread role in plant cell organization and function. *Nature Plants*, **8**, 670–681.

Lakkaraju, A.K., **Abrami, L.**, **Lemmin, T.**, **Blaskovic, S.**, **Kunz, B.**, **Kihara, A.** ***et al.*** (2012) Palmitoylated calnexin is a key component of the ribosome-translocon complex. *The EMBO Journal*, **31**, 1823–1835.

Langhorst, M.F., **Reuter, A.** & **Stuermer, C.A.** (2005) Scaffolding microdomains and beyond: the function of reggie/flotillin proteins. *Cellular and Molecular Life Sciences*, **62**, 2228–2240.

Lefebvre, B., **Batoko, H.**, **Duby, G.** & **Boutry, M.** (2004) Targeting of a *Nicotiana plumbaginifolia* H^+-ATPase to the plasma membrane is not by default and requires cytosolic structural determinants. *The Plant Cell*, **16**, 1772–1789.

Legrand, A., **G-Cava, D.**, **Jolivet, M.D.**, **Decossas, M.**, **Lambert, O.**, **Bayle, V.** ***et al.*** (2023) Structural determinants of remorin nanodomain formation in anionic membranes. *Biophysical Journal*, **122**, 2192–2202.

Legrand, A., **Martinez, D.**, **Grelard, A.**, **Berbon, M.**, **Morvan, E.**, **Tawani, A.** ***et al.*** (2019) Nanodomain clustering of the plant protein remorin by solid-state NMR. *Frontiers in Molecular Biosciences*, **6**, 107.

Levental, I., **Lingwood, D.**, **Grzybek, M.**, **Coskun, U.** & **Simons, K.** (2010) Palmitoylation regulates raft affinity for the majority of integral raft proteins. *Proceedings of the National Academy of Sciences of the United States of America*, **107**, 22050–22054.

Levet, F., **Hosy, E.**, **Kechkar, A.**, **Butler, C.**, **Beghin, A.**, **Choquet, D.** ***et al.*** (2015) SR-Tesseler: a method to segment and quantify localization-based super-resolution microscopy data. *Nature Methods*, **12**, 1065–1071.

Li, J., **Zhang, M.** & **Zhou, L.** (2022) Protein S-acyltransferases and acyl protein thioesterases, regulation executors of protein S-acylation in plants. *Frontiers in Plant Science*, **13**, 956231.

Li, R., **Liu, P.**, **Wan, Y.**, **Chen, T.**, **Wang, Q.**, **Mettbach, U.** ***et al.*** (2012) A membrane microdomain-associated protein, Arabidopsis Flot1, is involved in a clathrin-independent endocytic pathway and is required for seedling development. *Plant Cell*, **24**, 2105–2122.

Li, S., **Zhao, J.**, **Zhai, Y.**, **Yuan, Q.**, **Zhang, H.**, **Wu, X.** ***et al.*** (2019) The hypersensitive induced reaction 3 (HIR3) gene contributes to plant basal resistance via an EDS1 and salicylic acid-dependent pathway. *The Plant Journal*, **98**, 783–797.

Liang, P., **Stratil, T.F.**, **Popp, C.**, **Marin, M.**, **Folgmann, J.**, **Mysore, K.S.** ***et al.*** (2018) Symbiotic root infections in *Medicago truncatula* require remorin-mediated receptor stabilization in membrane nanodomains. *Proceedings of the National Academy of Sciences of the United States of America*, **115**, 5289–5294.

Liu, F., **Qu, P.Y.**, **Li, J.P.**, **Yang, L.N.**, **Geng, Y.J.**, **Lu, J.Y.** ***et al.*** (2024) Arabidopsis protein S-acyl transferases positively mediate BR signaling through S-acylation of BSK1. *Proceedings of the National Academy of Sciences of the United States of America*, **121**, e2322375121.

Liu, M.J., **Yeh, F.J.**, **Yvon, R.**, **Simpson, K.**, **Jordan, S.**, **Chambers, J.** ***et al.*** (2024) Extracellular pectin-RALF phase separation mediates FERONIA global signaling function. *Cell*, **187**, 312–330.e322.

Liu, X., **Li, M.**, **Li, Y.**, **Chen, Z.**, **Zhuge, C.**, **Ouyang, Y.** ***et al.*** (2021) An ABHD17-like hydrolase screening system to identify de-S-acylation enzymes of protein substrates in plant cells. *Plant Cell*, **33**, 3235–3249.

Liu, X., **Zhao, H.**, **Yuan, M.**, **Li, P.**, **Xie, J.**, **Fu, Y.** ***et al.*** (2024) An effector essential for virulence of necrotrophic fungi targets plant HIRs to inhibit host immunity. *Nature Communications*, **15**, 9391.

Lomize, A.L., **Todd, S.C.** & **Pogozheva, I.D.** (2022) Spatial arrangement of proteins in planar and curved membranes by PPM 3.0. *Protein Science*, **31**, 209–220.

Lopez Vazquez, A., **Allenbach Petrolati, L.**, **Legris, M.**, **Dessimoz, C.**, **Lampugnani, E.R.**, **Glover, N.** ***et al.*** (2023) Protein S-acylation controls the subcellular localization and biological activity of PHYTOCHROME KINASE SUBSTRATE. *Plant Cell*, **35**, 2635–2653.

Lupanga, U., **Rohrich, R.**, **Askani, J.**, **Hilmer, S.**, **Kiefer, C.**, **Krebs, M.** ***et al.*** (2020) The Arabidopsis V-ATPase is localized to the TGN/EE via a seed plant-specific motif. *eLife*, **9**, e60568.

Lv, X., **Jing, Y.**, **Xiao, J.**, **Zhang, Y.**, **Zhu, Y.**, **Julian, R.** ***et al.*** (2017) Membrane microdomains and the cytoskeleton constrain AtHIR1 dynamics and facilitate the formation of an AtHIR1-associated immune complex. *The Plant Journal*, **90**, 3–16.

Ma, C., **Wang, C.**, **Luo, D.**, **Yan, L.**, **Yang, W.**, **Li, N.** ***et al.*** (2022) Structural insights into the membrane microdomain organization by SPFH family proteins. *Cell Research*, **32**, 176–189.

Majeran, W., **Le Caer, J.P.**, **Ponnala, L.**, **Meinnel, T.** & **Giglione, C.** (2018) Targeted profiling of *Arabidopsis thaliana* subproteomes illuminates co- and posttranslationally N-terminal myristoylated proteins. *Plant Cell*, **30**, 543–562.

Mamode Cassim, A., **Gouguet, P.**, **Gronnier, J.**, **Laurent, N.**, **Germain, V.**, **Grison, M.** ***et al.*** (2019) Plant lipids: key players of plasma membrane organization and function. *Progress in Lipid Research*, **73**, 1–27.

Martin-Barranco, A., **Spielmann, J.**, **Dubeaux, G.**, **Vert, G.** & **Zelazny, E.** (2020) Dynamic control of the high-affinity iron uptake complex in root epidermal cells. *Plant Physiology*, **184**, 1236–1250.

Martinez, D., **Legrand, A.**, **Gronnier, J.**, **Decossas, M.**, **Gouguet, P.**, **Lambert, O.** ***et al.*** (2019) Coiled-coil oligomerization controls localization of the plasma membrane REMORINs. *Journal of Structural Biology*, **206**, 12–19.

Martiniere, A., **Fiche, J.B.**, **Smokvarska, M.**, **Mari, S.**, **Alcon, C.**, **Dumont, X.** ***et al.*** (2019) Osmotic stress activates two reactive oxygen species pathways with distinct effects on protein nanodomains and diffusion. *Plant Physiology*, **179**, 1581–1593.

Martiniere, A. & **Zelazny, E.** (2021) Membrane nanodomains and transport functions in plant. *Plant Physiology*, **187**, 1839–1855.

McKenna, J.F., **Rolfe, D.J.**, **Webb, S.E.D.**, **Tolmie, A.F.**, **Botchway, S.W.**, **Martin-Fernandez, M.L.** ***et al.*** (2019) The cell wall regulates dynamics and size of plasma-membrane nanodomains in Arabidopsis. *Proceedings of the National Academy of Sciences of the United States of America*, **116**, 12857–12862.

Mei, Y., **Ma, Z.**, **Wang, Y.** & **Zhou, X.** (2020) Geminivirus C4 antagonizes the HIR1-mediated hypersensitive response by inhibiting the HIR1 self-interaction and promoting degradation of the protein. *The New Phytologist*, **225**, 1311–1326.

Mesquita, F.S., **Abrami, L.**, **Sergeeva, O.**, **Turelli, P.**, **Qing, E.**, **Kunz, B.** ***et al.*** (2021) S-acylation controls SARS-CoV-2 membrane lipid organization and enhances infectivity. *Developmental Cell*, **56**, 2790–2807.e2798.

Moreau, H., **Zimmermann, S.D.**, **Gaillard, I.** & **Paris, N.** (2021) pH biosensing in the plant apoplast-a focus on root cell elongation. *Plant Physiology*, **187**, 504–514.

Neumann-Giesen, C., **Falkenbach, B.**, **Beicht, P.**, **Claasen, S.**, **Luers, G.**, **Stuermer, C.A.** ***et al.*** (2004) Membrane and raft association of reggie-1/flotillin-2: role of myristoylation, palmitoylation and oligomerization and induction of filopodia by overexpression. *Biochemical Journal*, **378**, 509–518.

Ning, W., **Jiang, P.**, **Guo, Y.**, **Wang, C.**, **Tan, X.**, **Zhang, W.** ***et al.*** (2021) GPS-Palm: a deep learning-based graphic presentation system for the prediction of S-palmitoylation sites in proteins. *Briefings in Bioinformatics*, **22**, 1836–1847.

Percher, A., **Thinon, E.** & **Hang, H.** (2017) Mass-tag labeling using acyl-PEG exchange for the determination of endogenous protein S-fatty acylation. *Current Protocols in Protein Science*, **89**, 14.17.1–14.17.11.

Perraki, A., **Cacas, J.L.**, **Crowet, J.M.**, **Lins, L.**, **Castroviejo, M.**, **German-Retana, S.** ***et al.*** (2012) Plasma membrane localization of *Solanum tuberosum* remorin from group 1, homolog 3 is mediated by conformational changes in a novel C-terminal anchor and required for the restriction of potato virus X movement. *Plant Physiology*, **160**, 624–637.

Platre, M.P., **Bayle, V.**, **Armengot, L.**, **Bareille, J.**, **Marques-Bueno, M.D.M.**, **Creff, A.** ***et al.*** (2019) Developmental control of plant rho GTPase nano-organization by the lipid phosphatidylserine. *Science*, **364**, 57–62.

Price, M.P., **Thompson, R.J.**, **Eshcol, J.O.**, **Wemmie, J.A.** & **Benson, C.J.** (2004) Stomatin modulates gating of acid-sensing ion channels. *The Journal of Biological Chemistry*, **279**, 53886–53891.

Qi, Y. & **Katagiri, F.** (2012) Membrane microdomain may be a platform for immune signaling. *Plant Signaling & Behavior*, **7**, 454–456.

Qi, Y., **Tsuda, K.**, **Nguyen Ie, V.**, **Wang, X.**, **Lin, J.**, **Murphy, A.S.** ***et al.*** (2011) Physical association of Arabidopsis hypersensitive induced reaction proteins (HIRs) with the immune receptor RPS2. *Journal of Biological Chemistry*, **286**, 31297–31307.

Raffaele, S., **Bayer, E.**, **Lafarge, D.**, **Cluzet, S.**, **German Retana, S.**, **Boubekeur, T.** ***et al.*** (2009) Remorin, a solanaceae protein resident in membrane rafts and plasmodesmata, impairs potato virus X movement. *Plant Cell*, **21**, 1541–1555.

Retzer, K., **Lacek, J.**, **Skokan, R.**, **Del Genio, C.I.**, **Vosolsobe, S.**, **Lankova, M.** ***et al.*** (2017) Evolutionary conserved cysteines function as cis-acting regulators of Arabidopsis PIN-FORMED 2 distribution. *International Journal of Molecular Sciences*, **18**, 2274.

Rivera-Milla, E., **Stuermer, C.A.** & **Malaga-Trillo, E.** (2006) Ancient origin of reggie (flotillin), reggie-like, and other lipid-raft proteins: convergent evolution of the SPFH domain. *Cellular and Molecular Life Sciences*, **63**, 343–357.

Schindelin, J., **Arganda-Carreras, I.**, **Frise, E.**, **Kaynig, V.**, **Longair, M.**, **Pietzsch, T.** ***et al.*** (2012) Fiji: an open-source platform for biological-image analysis. *Nature Methods*, **9**, 676–682.

Simon, M.L., **Platre, M.P.**, **Marques-Bueno, M.M.**, **Armengot, L.**, **Stanislas, T.**, **Bayle, V.** ***et al.*** (2016) A PtdIns(4)P-driven electrostatic field controls

cell membrane identity and signalling in plants. *Nature Plants*, **2**, 16089.

Singh, J., **Elhabashy, H.**, **Muthukottiappan, P.**, **Stepath, M.**, **Eisenacher, M.**, **Kohlbacher, O**. ***et al.*** (2022) Cross-linking of the endolysosomal system reveals potential flotillin structures and cargo. *Nature Communications*, **13**, 6212.

Smokvarska, M., **Bayle, V.**, **Maneta-Peyret, L.**, **Fouillen, L.**, **Poitout, A.**, **Dongois, A.** ***et al.*** (2023) The receptor kinase FERONIA regulates phosphatidylserine localization at the cell surface to modulate ROP signaling. *Science Advances*, **9**, eadd4791.

Smokvarska, M., **Francis, C.**, **Platre, M.P.**, **Fiche, J.B.**, **Alcon, C.**, **Dumont, X.** ***et al.*** (2020) A plasma membrane nanodomain ensures signal specificity during osmotic signaling in plants. *Current Biology*, **30**, 4654–4664.e4654.

Solis, G.P., **Hoegg, M.**, **Munderloh, C.**, **Schrock, Y.**, **Malaga-Trillo, E.**, **Rivera-Milla, E.** ***et al.*** (2007) Reggie/flotillin proteins are organized into stable tetramers in membrane microdomains. *Biochemical Journal*, **403**, 313–322.

Stoner, J., **Li, S.** & **Fu, Z.** (2025) Structural basis for membrane microdomain formation by a human stomatin complex. *Nature Communications*, **16**, 7439.

Tatsuta, T., **Model, K.** & **Langer, T.** (2005) Formation of membrane-bound ring complexes by prohibitins in mitochondria. *Molecular Biology of the Cell*, **16**, 248–259.

Ueda, T., **Yamaguchi, M.**, **Uchimiya, H.** & **Nakano, A.** (2001) Ara6, a plant-unique novel type Rab GTPase, functions in the endocytic pathway of *Arabidopsis thaliana*. *The EMBO Journal*, **20**, 4730–4741.

Umlauf, E., **Mairhofer, M.** & **Prohaska, R.** (2006) Characterization of the stomatin domain involved in homo-oligomerization and lipid raft association. *The Journal of Biological Chemistry*, **281**, 23349–23356.

Vangone, A. & **Bonvin, A.M.** (2015) Contacts-based prediction of binding affinity in protein-protein complexes. *eLife*, **4**, e07454.

Wang, B., **Zhou, Z.**, **Zhou, J.M.** & **Li, J.** (2024) Myosin XI-mediated BIK1 recruitment to nanodomains facilitates FLS2-BIK1 complex formation during innate immunity in Arabidopsis. *Proceedings of the National Academy of Sciences of the United States of America*, **121**, e2312415121.

Wattelet-Boyer, V., **Brocard, L.**, **Jonsson, K.**, **Esnay, N.**, **Joubes, J.**, **Domergue, F.** ***et al.*** (2016) Enrichment of hydroxylated C24- and C26-acyl-chain sphingolipids mediates PIN2 apical sorting at trans-Golgi network subdomains. *Nature Communications*, **7**, 12788.

Wright, K.J., **Baye, L.M.**, **Olivier-Mason, A.**, **Mukhopadhyay, S.**, **Sang, L.**, **Kwong, M.** ***et al.*** (2011) An ARL3-UNC119-RP2 GTPase cycle targets myristoylated NPHP3 to the primary cilium. *Genes & Development*, **25**, 2347–2360.

Xue, L.C., **Rodrigues, J.P.**, **Kastritis, P.L.**, **Bonvin, A.M.** & **Vangone, A.** (2016) PRODIGY: a web server for predicting the binding affinity of protein-protein complexes. *Bioinformatics*, **32**, 3676–3678.

Yu, M., **Liu, H.**, **Dong, Z.**, **Xiao, J.**, **Su, B.**, **Fan, L.** ***et al.*** (2017) The dynamics and endocytosis of Flot1 protein in response to flg22 in Arabidopsis. *Journal of Plant Physiology*, **215**, 73–84.

Zelazny, E., **Santambrogio, M.**, **Pourcher, M.**, **Chambrier, P.**, **Berne-Dedieu, A.**, **Fobis-Loisy, I.** ***et al.*** (2013) Mechanisms governing the endosomal membrane recruitment of the core retromer in Arabidopsis. *The Journal of Biological Chemistry*, **288**, 8815–8825.

Zhang, Y.L., **Li, E.**, **Feng, Q.N.**, **Zhao, X.Y.**, **Ge, F.R.**, **Zhang, Y.** ***et al.*** (2015) Protein palmitoylation is critical for the polar growth of root hairs in Arabidopsis. *BMC Plant Biology*, **15**, 50.

Zhou, L., **Cheung, M.Y.**, **Zhang, Q.**, **Lei, C.L.**, **Zhang, S.H.**, **Sun, S.S.** ***et al.*** (2009) A novel simple extracellular leucine-rich repeat (eLRR) domain protein from rice (OsLRR1) enters the endosomal pathway and interacts with the hypersensitive-induced reaction protein 1 (OsHIR1). *Plant, Cell & Environment*, **32**, 1804–1820.

Zhu, X.G., **Nicholson Puthenveedu, S.**, **Shen, Y.**, **La, K.**, **Ozlu, C.**, **Wang, T.** ***et al.*** (2019) CHP1 regulates compartmentalized glycerolipid synthesis by activating GPAT4. *Molecular Cell*, **74**, 45–58.e47.